Neuron

NeuroResource

Distinct systemic impacts of Aβ42 and Tau revealed by whole-organism snRNA-seq

Graphical abstract

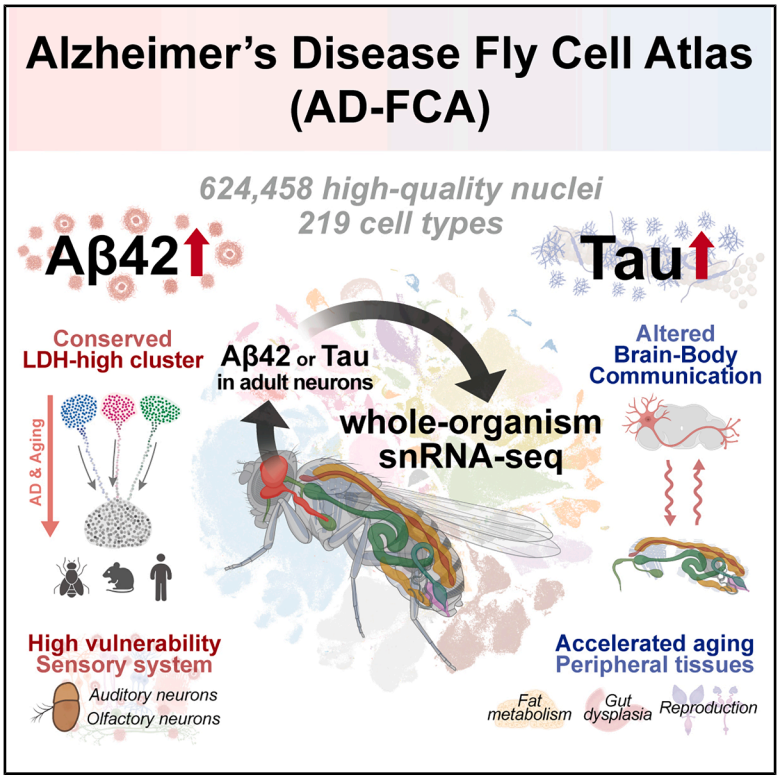

Highlights

- AD-FCA includes 624,458 nuclei covering 219 cell types from whole organism
- Neuronal Aβ42 and Tau display distinct impacts
- Aβ42 primarily affects sensory systems and induces a conserved LDH-high cluster
- Tau induces accelerated aging in the periphery and alters brain-body communications

Authors

Ye-Jin Park, Tzu-Chiao Lu, Tyler Jackson, ..., Yanyan Qi, Hugo J. Bellen, Hongjie Li

Correspondence

hbellen@bcm.edu (H.J.B.), hongjie.li@bcm.edu (H.L.)

In brief

Park and Lu et al. create a whole-organism Alzheimer's disease (AD) Fly Cell Atlas to reveal how AD-associated proteins systemically affect the brain and body. Their work uncovers distinct effects of Aβ42 and Tau and highlights disrupted brain-body communications as a feature of neurodegeneration.

Park et al., 2025, Neuron *113*, 1–18
July 9, 2025
https://doi.org/10.1016/j.neuron.2025.04.017

CellPress

Neuron

CellPress

NeuroResource

Distinct systemic impacts of Aβ42 and Tau revealed by whole-organism snRNA-seq

Ye-Jin Park,[1,2,3,4,12] Tzu-Chiao Lu,[1,2,12] Tyler Jackson,[1,2,5] Lindsey D. Goodman,[2,3] Lindsey Ran,[1,2] Jiaye Chen,[1,2] Chung-Yi Liang,[1,2,6] Erin Harrison,[1,2] Christina Ko,[1,2] Xi Chen,[7] Baiping Wang,[1,2] Ao-Lin Hsu,[6,8] Elizabeth Ochoa,[9] Kevin F. Bieniek,[9,10] Shinya Yamamoto,[2,3,4,11] Yi Zhu,[7] Hui Zheng,[1,2,11] Yanyan Qi,[1,2] Hugo J. Bellen,[2,3,4,11,*] and Hongjie Li[1,2,13,*]

[1]Huffington Center on Aging, Baylor College of Medicine, Houston, TX 77030, USA
[2]Department of Molecular and Human Genetics, Baylor College of Medicine, Houston, TX 77030, USA
[3]Jan and Dan Duncan Neurological Research Institute, Texas Children's Hospital, Houston, TX 77030, USA
[4]Program in Development, Disease Models & Therapeutics, Baylor College of Medicine, Houston, TX 77030, USA
[5]Program in Cancer Cell Biology, Baylor College of Medicine, Houston, TX 77030, USA
[6]Institute of Biochemistry and Molecular Biology, National Yang Ming Chiao Tung University, Taipei 11221, Taiwan
[7]USDA/ARS Children's Nutrition Research Center, Department of Pediatrics, Baylor College of Medicine, Houston, TX 77030, USA
[8]Department of Internal Medicine, Division of Geriatric and Palliative Medicine, University of Michigan, Ann Arbor, MI 28109, USA
[9]Glenn Biggs Institute for Alzheimer's & Neurodegenerative Diseases, UT Health San Antonio, San Antonio, TX 78229, USA
[10]Department of Pathology & Laboratory Medicine, UT Health San Antonio, San Antonio, TX 78229, USA
[11]Department of Neuroscience, Baylor College of Medicine, Houston, TX 77030, USA
[12]These authors contributed equally
[13]Lead contact
*Correspondence: hbellen@bcm.edu (H.J.B.), hongjie.li@bcm.edu (H.L.)
https://doi.org/10.1016/j.neuron.2025.04.017

SUMMARY

Both neuronal and peripheral tissues become disrupted in Alzheimer's disease (AD). However, a comprehensive understanding of how AD impacts different tissues across the whole organism is lacking. Using *Drosophila*, we generated an AD Fly Cell Atlas (AD-FCA) based on whole-organism single-nucleus transcriptomes of 219 cell types from flies expressing AD-associated proteins, either human amyloid-β 42 peptide (Aβ42) or Tau, in neurons. We found that Aβ42 primarily affects the nervous system, including sensory neurons, while Tau induces accelerated aging in peripheral tissues. We identified a neuronal cluster enriched in Aβ42 flies, which has high lactate dehydrogenase (LDH) expression. This LDH-high cluster is conserved in 5XFAD mouse and human AD datasets. We found a conserved defect in fat metabolism from both fly and mouse tauopathy models. The AD-FCA offers new insights into how Aβ42 or Tau systemically and differentially affects a whole organism and provides a valuable resource for understanding brain-body communication in neurodegeneration.

INTRODUCTION

Alzheimer's disease (AD) has been extensively investigated, with a predominant focus on the central nervous system (CNS). Amyloid plaques (composed of Aβ peptides) and neurofibrillary tangles (composed of hyperphosphorylated Tau) in the brain are hallmarks of AD, and most studies focus on the impact on neurons.[1] However, emerging evidence indicates that the effects of AD extend beyond the CNS to peripheral organs. For example, AD has been associated with disruptions in the gut microbiota, cardiovascular function, and hormone homeostasis.[2–5] Moreover, peripheral inflammation and immune decline can contribute to AD pathogenesis.[6] Hence, a comprehensive comparison across all cell types is needed to provide important insights into AD and to understand whether peripheral defects contribute to neurological features in disease versus being the result of neurodegeneration.

The fruit fly, *Drosophila melanogaster*, is a prime experimental model for studying aging and age-related diseases, including AD.[7–10] Many molecular pathways are conserved from flies to mammals and were initially characterized using *Drosophila*.[11,12] Advances in single-cell RNA sequencing (scRNA-seq) have promoted its use in defining new cell types and progressive changes in individual cell types during aging.[13–19] Our whole-organism single-nucleus RNA sequencing (snRNA-seq) platform led to the development of the Fly Cell Atlas (FCA),[15] as well as the Aging Fly Cell Atlas (AFCA),[16] a comprehensive single-cell transcriptomic dataset interrogating aging features in *Drosophila*.

Here, we apply this approach to AD and present the AD-FCA. The AD-FCA profiles single-nucleus transcriptomes from the

Please cite this article in press as: Park et al., Distinct systemic impacts of Aβ42 and Tau revealed by whole-organism snRNA-seq, Neuron (2025), https://doi.org/10.1016/j.neuron.2025.04.017

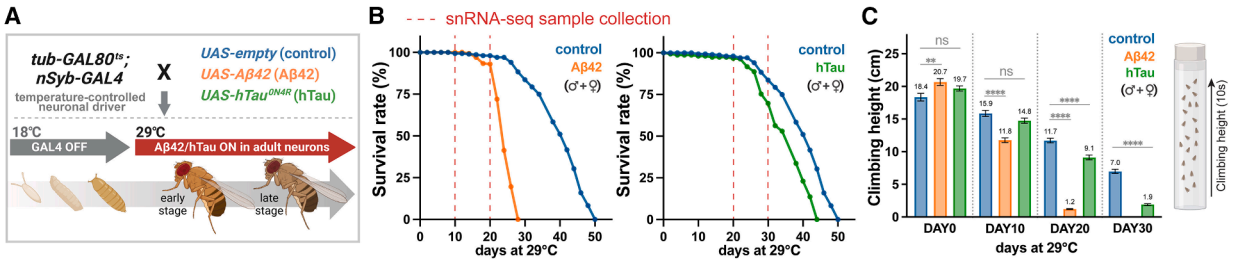

D

control	10d	20d	30d
	male-head	male-head	male-head
	male-body	male-body	male-body
	female-head	female-head	female-head
	female-body	female-body	female-body
Aβ42	10d (early)	20d (late)
	male-head	male-head
	male-body	male-body
	female-head	female-head
	female-body	female-body
hTau	20d (early)	30d (late)
	male-head	male-head
	male-body	male-body
	female-head	female-head
	female-body	female-body

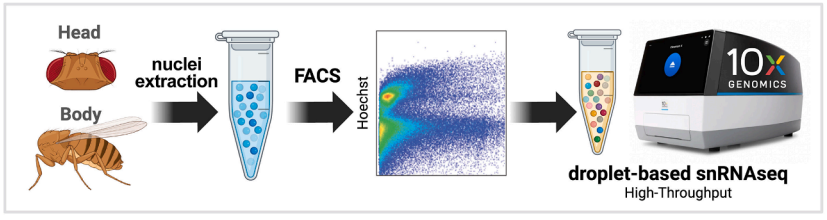

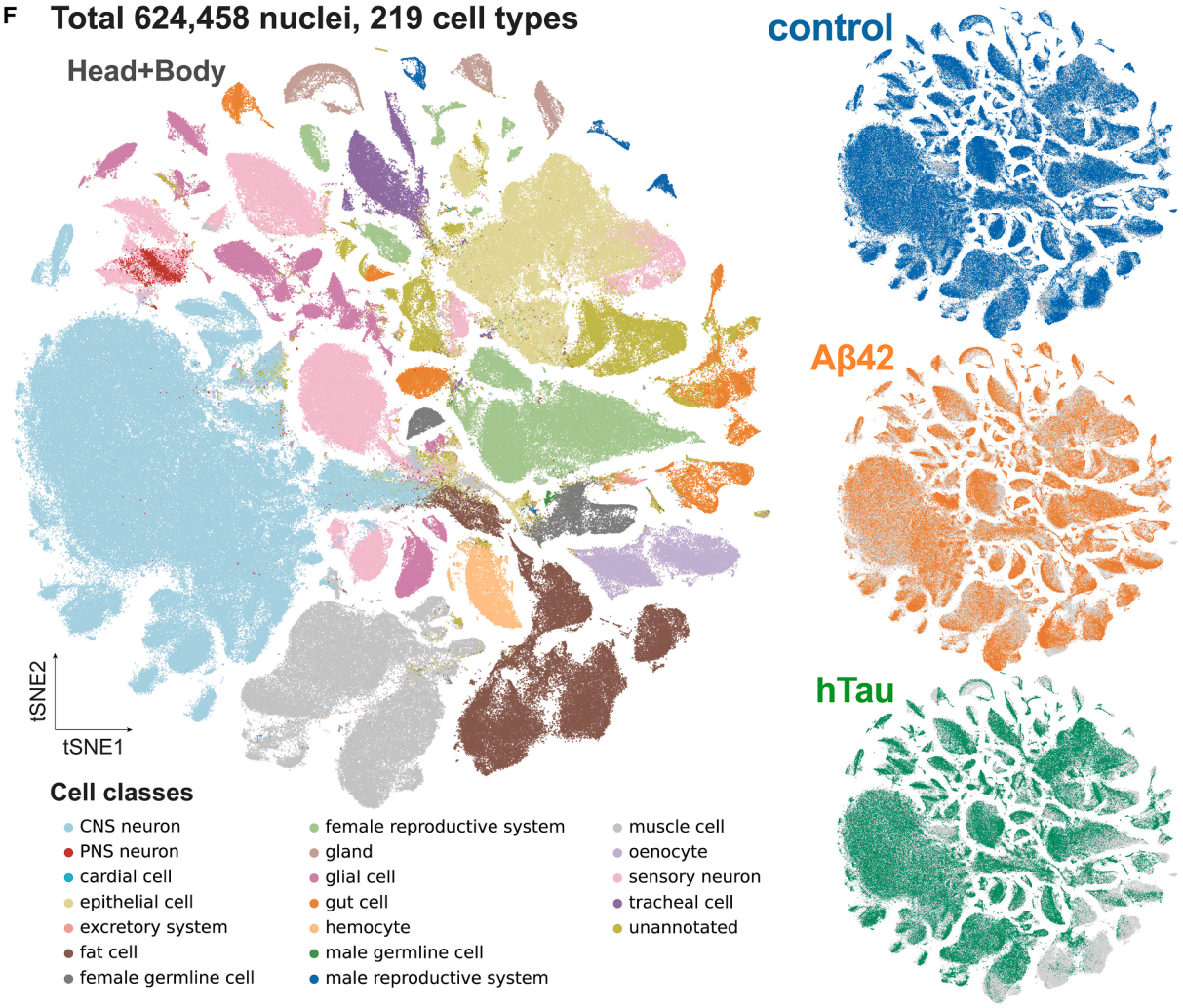

(legend on next page)

Please cite this article in press as: Park et al., Distinct systemic impacts of Aβ42 and Tau revealed by whole-organism snRNA-seq, Neuron (2025), https://doi.org/10.1016/j.neuron.2025.04.017

whole fly upon expression of either secreted amyloid-β 42 peptide (Aβ42) or wild-type human Tau (hTau) in neurons (hereafter, referred to as Aβ42 flies and hTau flies). Aβ42 flies and hTau flies display disease-associated phenotypes, including reduced lifespan, climbing defects, and neuronal cell loss.[20–24] Our AD-FCA and *in vivo* data revealed that neuronal Aβ42 primarily impacts neurons, with sensory neurons being particularly susceptible. We also discovered a lactate dehydrogenase (LDH)-high neuronal cluster composed of multiple neuronal subtypes, which is not only observed in flies but also in mouse and human snRNA-seq data. By contrast, neuronal hTau impacts many non-neuronal peripheral cell types, including gut, fat body, and reproductive system. Interestingly, many of the peripheral changes mimic age-associated phenotypes, suggesting that neuronal expression of hTau causes accelerated aging in peripheral tissues.

This AD-FCA provides a valuable resource for the neurodegeneration research community. It enables us to uncover systemic and conserved changes that occur in neuronal and non-neurological tissues, offering new insights into the realm of brain-body communication. All data can be accessed through the visualization and analysis portal at https://hongjielilab.org/adfca/ (Figures S1J and S4).

RESULTS

Whole-organism single-nucleus transcriptomes of flies expressing Aβ42 or hTau in neurons

To generate the AD-FCA, we used a temperature-controlled pan-neuronal GAL4 system (*tub-GAL80^{ts}; nSyb-GAL4*) that restricts the expression of Aβ42 (*UAS-Aβ42*) or hTau (*UAS-hTau^{0N4R}*) to adult fly neurons, avoiding developmental effects (Figure 1A). We selected established AD fly models that have been well characterized and used to reveal conserved disease mechanisms.[20–24] To minimize the genetic background effect, we expressed *UAS-empty* in control flies. Aβ42 or hTau expression in the brain was confirmed by immunofluorescence staining (Figures S1A and S1B). Lifespan and negative geotaxis assays were used to define early and late time points of phenotypic progression, and flies from these time points were selected for profiling (Figures 1B, 1C, and S1C–S1F). Aβ42 flies were collected at day 10 (early) and 20 (late), whereas hTau flies were collected at days 20 (early) and 30 (late). Control flies were collected at all three ages (days 10, 20, and 30). We performed droplet-based snRNA-seq on whole heads and whole bodies, separating males and females (Figure 1D). We followed our previous snRNA-seq pipeline[15,16] except that high-throughput kits were used to improve nuclei yield and gene detection (Figures 1E and S1G–S1I). In total, we obtained 624,458 high-quality nuclei covering 18 broad cell classes (Figure 1F).

Next, we employed a supervised machine learning-based method for annotating the cell types using previous datasets as references, including the FCA, AFCA, and a fly optical lobe dataset.[15,16,25] We manually validated each annotation using cell-type-specific markers. Overall, we identified 219 different cell types (Figures 1F, S2, and S3).

Sensory neurons of the head are vulnerable cell types in Aβ42 flies

We next performed a comprehensive comparison among all cell types from the fly head, including CNS neurons, peripheral nervous system (PNS) neurons, glia, and other non-neural cells (Figure 2A). Unless otherwise specified, samples from early and late time points (Figure 1D) for both sexes were combined and compared against age-matched controls.

First, we assessed the cellular composition (see STAR Methods). Because there is limited neurogenesis or gliosis in adult fly brains,[26] we anticipated that cellular composition changes would be caused by cell loss. Our snRNA-seq data revealed that Aβ42, but not hTau, causes a decrease in the nuclear ratio of many cell types (Figure S5B). Consistently, Aβ42 fly brains show more vacuolization than control or hTau flies (Figure S5A). Among the top ten most affected cell types in Aβ42 fly heads are seven types of CNS neurons, two types of sensory neurons, and one glial cell type (Figures 2B, 2C, and S5B). Interestingly, all these cell types are directly associated with sensory functions, including vision, audition, and olfaction (Figure 2C), suggesting that the sensory system is more vulnerable to Aβ42 expression. Second, we performed differentially expressed gene (DEG) analysis to compare Aβ42 or hTau flies with the corresponding controls (Figure S5C). Three types of sensory neurons, including outer photoreceptors (R1–R6), auditory sensory neurons (ASNs), and olfactory receptor neurons (ORNs), are among the top cell types with the highest number of DEGs in Aβ42 flies (Table S1). We also observed that Aβ42 or hTau expression caused different DEG patterns. For example, in ASNs, Aβ42 showed 371 DEGs, while hTau only showed 16 DEGs.

We observed a significant reduction in the number of ASN nuclei in Aβ42 flies when compared with control flies (Figure 2D), consistent with our snRNA-seq data. This reduction is not due to the differential expression of the *GAL4/UAS* system

Figure 1. Overview of the AD-FCA

(A) Fly models of AD-FCA.

(B) Survival curves at 29°C. Female and male flies were counted separately and combined for generating the survival curves. $n = 300$ (150 female and 150 male) per genotype. See separate lifespan curves in Figure S1.

(C) Climbing defects observed in Aβ42 and hTau flies compared with controls. Bars represent mean ± SEM. $^{**}p \leq 0.01$, $^{****}p \leq 0.0001$. p values were from parametric unpaired t test. The numbers above the bars indicate mean values. Female and male flies were counted separately. See Figure S1.

(D) Summary of samples collected from three genotypes.

(E) Flowchart of the snRNA-seq experiment. Fluorescence-activated cell sorting (FACS) was used to sort nuclei.

(F) t-distributed stochastic neighbor embedding (tSNE) visualizations showing 18 broad cell classes integrated across different samples (left). tSNE visualizations separated by genotype (right).

Please cite this article in press as: Park et al., Distinct systemic impacts of Aβ42 and Tau revealed by whole-organism snRNA-seq, Neuron (2025), https://doi.org/10.1016/j.neuron.2025.04.017

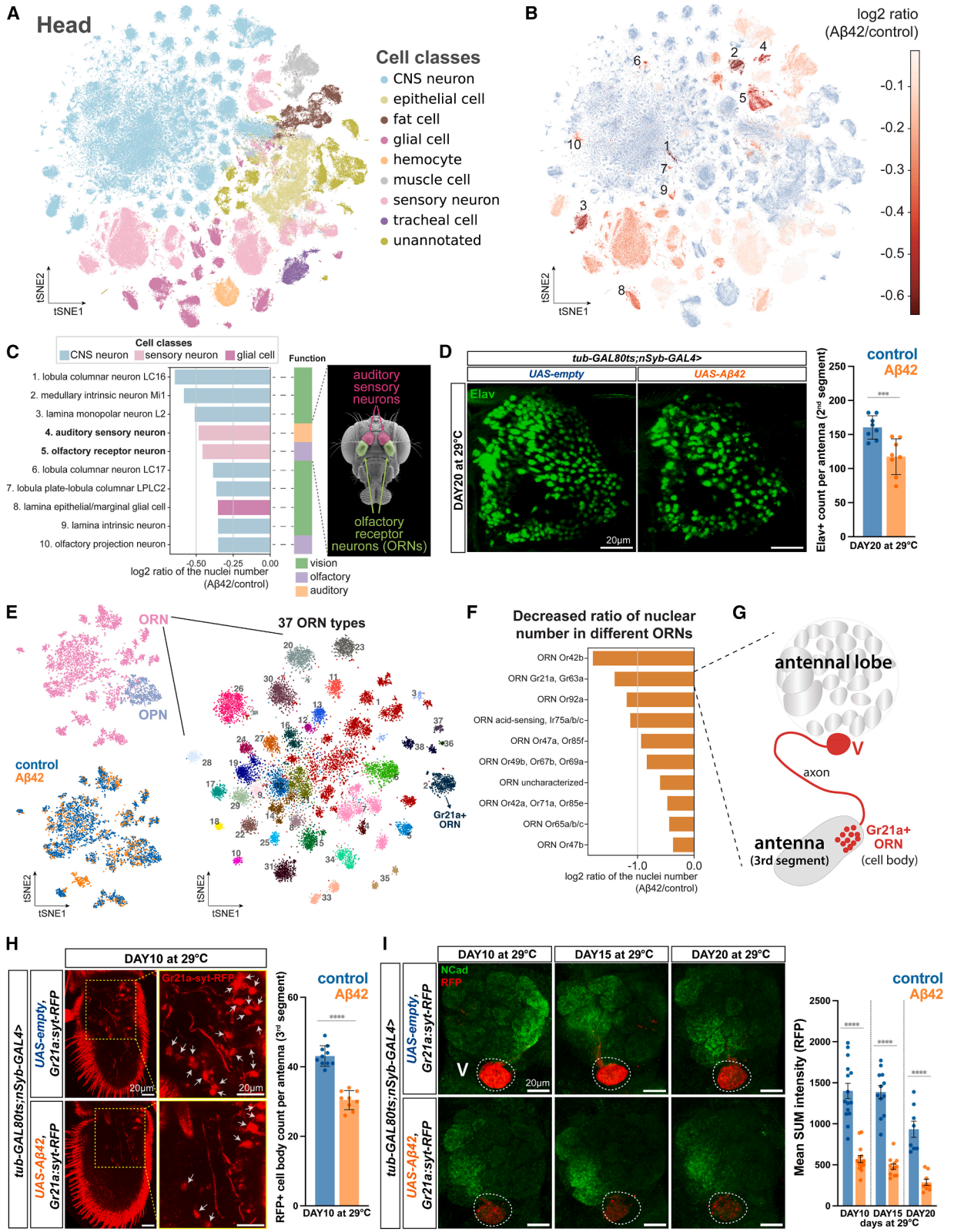

(legend on next page)

Please cite this article in press as: Park et al., Distinct systemic impacts of Aβ42 and Tau revealed by whole-organism snRNA-seq, Neuron (2025), https://doi.org/10.1016/j.neuron.2025.04.017

used to express Aβ42 (Figures S5D and S5E). Hence, ASNs are susceptible to Aβ42-associated toxicity.

Olfactory sensory decline is an early symptom in human AD.[27] However, it is largely unknown which neurons in a sensory circuit are primarily affected in AD. Flies have about 50 pairs of ORNs (PNS neurons) and secondary olfactory project neurons (OPNs, CNS neurons).[28] Interestingly, we found that ORNs are more affected than OPNs based on both cell loss and DEG analyses (Figure 2C, S5B, and S5C). Next, we sub-clustered all ORNs into 37 distinct clusters that express specific olfactory receptors (Figures 2E and S5F). Ranking these ORN subtypes based on cell composition analysis showed that *Or42b*-expressing ORNs (detect vinegar[29]) and *Gr21a/Gr63a*-expressing ORNs (detect CO_2[30]) are most affected (Figure 2F). To validate this, we expressed *Gr21a:syt-RFP*[31] in Aβ42 and control flies. We found that both cell body numbers and axon terminal signals of *Gr21a/Gr63a*-ORNs are significantly decreased in Aβ42 flies (Figures 2G–2I).

In summary, these analyses indicate that sensory systems are particularly susceptible to Aβ42. This is consistent with several studies showing that olfactory decline is one of the earliest symptoms in AD patients.[32,33]

LDH-high cluster in Aβ42 flies

Next, we sought to identify possible mechanisms for Aβ42-induced neuronal loss. We observed an Aβ42-dominant neuronal cluster characterized by a high level of *Ldh* transcripts, which we named the LDH-high cluster (Figures 3A–3C and S6A–S6C). There are two possible origins for this cluster: (1) the cells arise from a certain neuronal type, or (2) these cells represent different types of neurons that converge to a similar transcriptional state due to Aβ42 expression.

To assess these possibilities, we expressed an *Ldh-GFP* reporter[34] in control, Aβ42, and hTau flies. Aβ42 flies exhibit a significant increase in Ldh-GFP across different brain regions and the antenna when compared with control or hTau flies (Figures 3D, 3E, S6D, and S6E). This widespread distribution of Ldh-GFP signal is further supported by our snRNA-seq data, which show that neurons within the LDH-high cluster express *VaChT* (cholinergic neurons), *Gad1* (GABAergic neurons), and *VGlut* (glutamatergic neurons) (Figure 3F), demonstrating that the LDH-high cluster comprises different neuronal types. Additionally, we performed sub-clustering analysis on the LDH-high cluster with two distinct neuronal types, lamina monopolar neuron L2 (L2) and medullary intrinsic neuron Mi1 (Mi1), which are highly impacted in Aβ42 flies (see Figure 2C). Interestingly, both L2 and Mi1 clusters form a bridge-like pattern connecting them with the LDH-high cluster (Figure 3G). Expression of markers in the LDH-high cluster (*Hsc70-3*), L2 neuron (*CG13739*), or Mi1 neuron (*Octbeta1R*) showed that these genes are expressed in these "bridge" cells (Figure 3H). Altogether, our data suggest that cells in the LDH-high cluster originate from many different types of neurons.

Next, we assessed the possible correlation between Aβ42 accumulation and Ldh expression. Extracellular Aβ42 was enriched in specific brain regions, including the antennal lobe and Kenyon cells of the mushroom body, the latter being the fly's memory center[35] (Figures S6E–S6G). Unexpectedly, these brain regions in Aβ42 flies show different degrees of Ldh-GFP expression: high in the antennal lobe and low in the mushroom body. Further, areas with moderate Aβ42 accumulation can exhibit prevalent Ldh-GFP signals (Figures S6F and S6G). Interestingly, Ldh-GFP expression emerges in distinct glomeruli at different time points (Figure S6G), supporting the idea that ORN susceptibility to Aβ42 varies by subtype (Figure 2F). These observations indicate that Aβ42 accumulation does not directly correlate with Ldh-GFP expression.

ER stress response in Aβ42 flies

We next performed Gene Ontology (GO) analysis on DEGs from the LDH-high cluster (Figure S7A; Table S2). The top GO terms are all related to neuronal function with one exception, "response to endoplasmic reticulum (ER) stress." Representative genes in this GO term include *Hsc70-3*, *CaBP1*, *ERp60*, *PHGPx*, *Xbp1*, and *cnc*, all displaying higher expression levels in the top affected cell types from Aβ42 flies (Figures 3I and S7B). We confirmed that Hsc70-3 protein levels are increased in Aβ42 flies using an anti-BiP (Hsc70-3) antibody (Figures 3J and S7C). BiP-positive cells in Aβ42 fly brains are localized across different regions, consistent with the broad staining pattern of Ldh-GFP (see Figure 3D).

Figure 2. Cell vulnerability in the head of Aβ42 flies

(A) tSNE visualizations of head samples showing broad cell classes.

(B) Decrease of nuclear ratios in Aβ42 flies. Nuclear ratios are compared between Aβ42 and control flies, and the top 10 cell types with the biggest decrease are marked. Numbered cell types are shown in (C).

(C) The top 10 cell types with the biggest decrease of nuclear ratios in Aβ42 flies. The cartoon illustrates the locations of two types of sensory neurons.

(D) Elav staining of ASN nuclei in the 2nd segment of the antenna. Elav+ nuclei were counted from whole z series images. $n = 8$ per genotype. Scatterplot with bar (mean ± SD).

(E) tSNE visualization of ORN and OPN. Both clusters are shown with corresponding cell types and genotypes (left). ORNs are further sub-clustered (right). See Figure S5F for annotation and corresponding marker genes.

(F) Top 10 ORN subtypes with the biggest decrease of nuclear ratios among ORNs in Aβ42 flies.

(G) Schematic of *Gr21a*+ ORN cell bodies and axon projection (red). *Gr21a*+ ORNs project their axons to the V (ventral) region of the antennal lobe in the brain.

(H) Comparison of *Gr21a*+ ORN cell body counts between Aβ42 and control flies. The RFP+ cell bodies (red) were counted from whole z series images. Control ($n = 10$), Aβ42 ($n = 9$). Scatterplot with bar (mean ± SD). The representative images were generated by the MAX intensity of Z planes containing these cell bodies. The off-target signal detected outside of the yellow dotted box region is due to the laser reflection on the cuticle.

(I) Comparison of axon terminal signals of *Gr21a*+ ORNs between Aβ42 and control flies. Anti-RFP (red, Gr21a+ ORN axon terminal) and anti-NCad (green, neuropil of the antennal lobe). $n = 8$–15 per genotype/age. Scatterplot with bar (mean ± SEM).

p values in (D), (H), and (I) were computed using the parametric unpaired t test. $^{***}p \leq 0.001$, $^{****}p \leq 0.0001$. For (D) and (I), representative images were generated by the maximum (MAX) intensity projection of all Z planes.

Please cite this article in press as: Park et al., Distinct systemic impacts of Aβ42 and Tau revealed by whole-organism snRNA-seq, Neuron (2025), https://doi.org/10.1016/j.neuron.2025.04.017

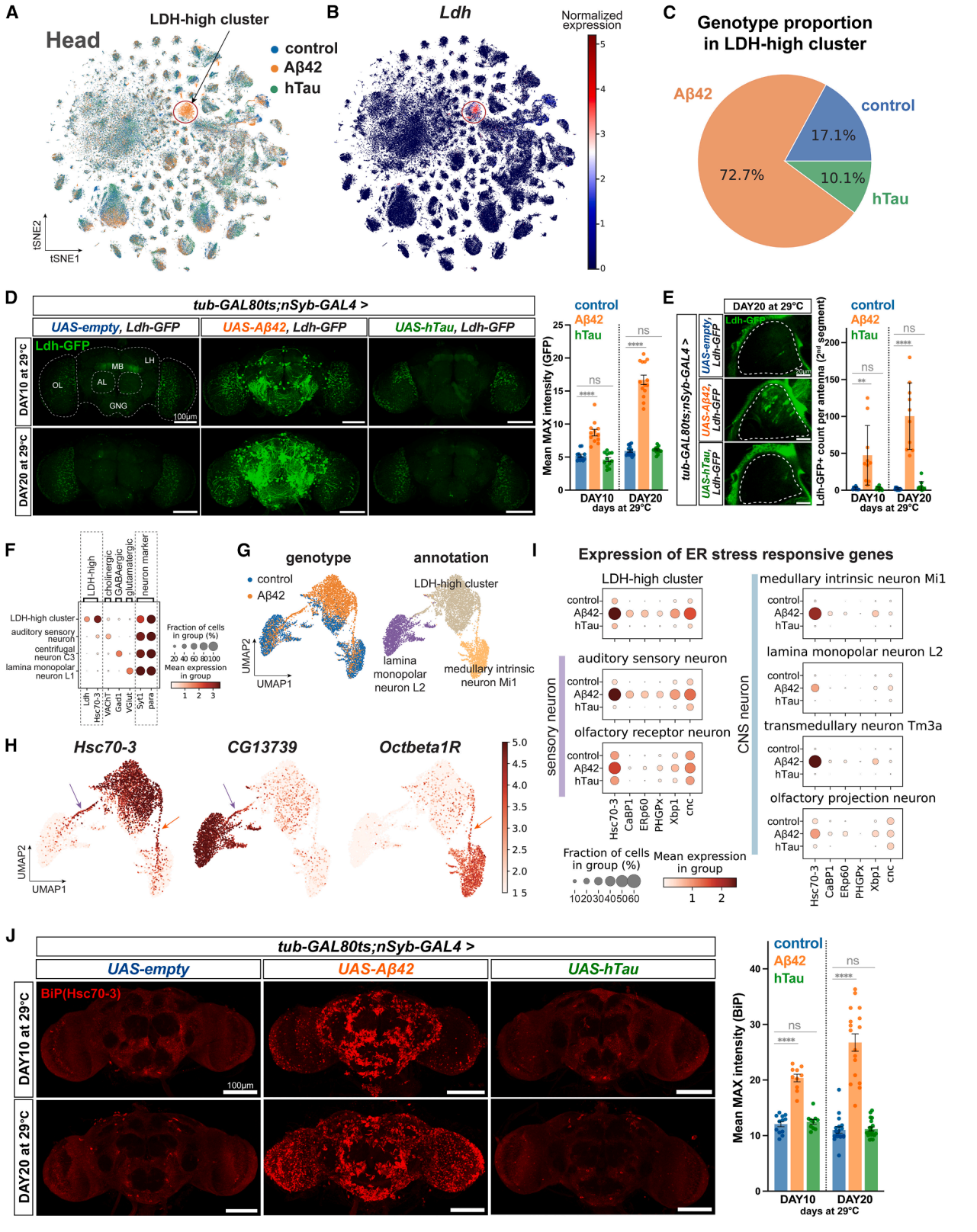

(legend on next page)

Please cite this article in press as: Park et al., Distinct systemic impacts of Aβ42 and Tau revealed by whole-organism snRNA-seq, Neuron (2025), https://doi.org/10.1016/j.neuron.2025.04.017

Ldh and *Hsc70-3* expression within the whole brain gradually increases with age in Aβ42 flies, raising the question of whether certain cell types respond to Aβ42 earlier than others (Figures 3D and 3J). To investigate this, we grouped samples by age and identified stage-specific DEGs. Among neurons with the highest DEGs, we observed a greater number of DEGs at the late stage, suggesting that the transcriptome becomes progressively altered (Figure S7D, upper). A consistent pattern was observed when we examined the ratio of early-stage to late-stage DEGs (Figure S7D, lower). Here, we observed that the LDH-high cluster exhibited the lowest early-to-late DEG ratio, highlighting that this cluster gradually accumulates. By contrast, ASNs showed the highest early-to-late DEG ratio, suggesting a rapid response to Aβ42. GO analysis further revealed gradual shifts in biological processes, including the previously identified ER stress response (Figure S7E). Additionally, ASNs exhibited the highest levels of ER stress-related genes in the early stage, further indicating their prompt response to Aβ42 (Figure S7F).

It has been shown that persistent activation of ER stress can lead to cell death,[36] while a potential contribution of ER stress to AD progression is of interest.[37] We found that a cell death-associated GO term and an apoptosis-related gene, *Calr*,[38] are significantly enriched in ASNs in addition to ER stress-related genes (Figures S7E–S7G). *Calr* is also highly enriched in the LDH-high cluster (Figure S7G). We also observed high levels of cleaved caspase-3 in Aβ42 brains (Figure S7H). Furthermore, many cells exhibiting a strong ER stress response (BiP-positive cells) in Aβ42 brains are also positive for cleaved caspase-3 (Figures S7H and S7I), suggesting a potential link between Aβ42-induced ER stress and neuronal apoptosis.

Identification of the conserved LDH-high cluster in mouse and human AD snRNA-seq datasets

We next aimed to determine if the LDH-high cluster is conserved in 5XFAD mice, a commonly used model to study amyloid pathology[39] and AD-derived cortical tissue. We first calculated the LDH-module score using the top 10 markers from the fly LDH-high cluster (Figure 4A; Table S2; see STAR Methods). These scores were then applied to a 5XFAD mouse cortex snRNA-seq dataset[40] and two independent human AD datasets, publicly available snRNA-seq datasets derived from human AD prefrontal cortical tissue that contain 26 (median age 83 years) or 427 (median age 88 years) subjects, respectively.[41,42] Consistently, we identified an LDH-high cluster in both mouse and human datasets (Figures 4B, 4C, S8A, S8B, S8E, S8F, and S9A). This cluster of cells was previously annotated as excitatory neurons, likely due to the high prevalence of excitatory neurons in the samples.

We observe several conserved features between the fly and human LDH-high clusters. First, this cluster in the human datasets is composed of multiple neuronal types, including different excitatory neuron subtypes (Figures 4D, S8C, S8D, S8G, and S8H). Second, the bridge cells observed in the fly model were also present in human AD samples (Figure 4D). Third, the LDH-high cluster is absent in young, non-AD human brains (3 subjects, ages 29, 42, and 50 years), whereas excitatory neuron subtype-specific gene expression remains (Figures S9C–S9E).[18] Similarly, the fly LDH-high cluster contains very few cells from young control flies (Figure S9F). These data suggest that aging and AD progression are crucial for the formation of this LDH-high cluster (Figure 4E). Fourth, we observed 233 conserved genes enriched in both fly and human LDH-high clusters (Figure 4F; Table S2). Of interest, one of the prominent terms from GO analysis is "response to unfolded protein" (Figure 4G). The unfolded protein response (UPR) is a cellular stress pathway associated with ER stress.[43,44] In the human LDH-high cluster, UPR and/or ER stress-related genes such as *NFE2L1* (fly *cnc* ortholog) and *ATF4* are notably upregulated (Figures S8B, S8F, and S9A). Hence, cells within the LDH-high cluster from both fly and human have conserved transcriptional changes, including increased UPR/ER-stress-associated genes.

To further assess the LDH-high cluster in humans, we performed GO analysis on all 1,063 upregulated DEGs from this human LDH-high cluster. We observed significant alterations in genes encoding mitochondrial respiratory functions (Figures 4H and S8I). This included several respiratory genes associated with AD,[45–48] including *ATP5F1D, UQCRC1*, and *NDUFB8* (Figure 4H, right). These data support the notion that this LDH cluster has pathological significance, as mitochondrial dysfunction is associated with oxidative stress, an early feature

Figure 3. Characterization of the LDH-high cluster

(A) The tSNE plot colored by different genotypes with the LDH-high cluster circled.

(B) The expression of *Ldh* enriched in the LDH-high cluster.

(C) Genotype proportion in LDH-high cluster.

(D and E) Enhanced Ldh-GFP (green) in Aβ42 brains (D) and ASNs (E) compared with control and hTau flies. (D) The mean GFP signal intensity/area in the whole brain was quantified from MAX intensity images. n = 12–15 per genotype/age. Scatterplot with bar (mean ± SEM). OL, optic lobe; AL, antennal lobe; MB, mushroom body; LH, lateral horn; GNG, gnathal ganglia. (E) The GFP+ cell bodies were counted from whole z series images. n = 10–12 per genotype/age. Scatterplot with bar (mean ± SD). The representative images were generated by the MAX intensity of Z planes containing these cell bodies. The off-target signal detected outside of the circled region is due to the laser reflection on the cuticle.

(F) Dot plot showing markers that are specific to the LDH-high cluster and three types of neurons, as well as two pan-neuronal marker genes.

(G) Co-clustering of the LDH-high cluster and two other neuronal types. Here, we employed uniform manifold approximation and projection (UMAP) instead of tSNE to enhance the visualization of transitional cell populations.

(H) UMAPs showing the expression of marker genes specific to the LDH-high cluster, L2, and Mi1 cells. Bridge cells are indicated by arrows.

(I) Expression of ER stress-responsive genes.

(J) Immunofluorescence analysis of BiP/Hsc70-3 in the whole brain. The mean BiP signal intensity/area in the whole brain was quantified from MAX intensity images. n = 10–20 per genotype/age. Scatterplot with bar (mean ± SEM).

p values in (D), (E), and (J) were computed using the parametric unpaired t test. $^{**}p \leq 0.01$, $^{****}p \leq 0.0001$. For (D) and (J), representative images were generated by the MAX intensity of all Z planes.

Please cite this article in press as: Park et al., Distinct systemic impacts of Aβ42 and Tau revealed by whole-organism snRNA-seq, Neuron (2025), https://doi.org/10.1016/j.neuron.2025.04.017

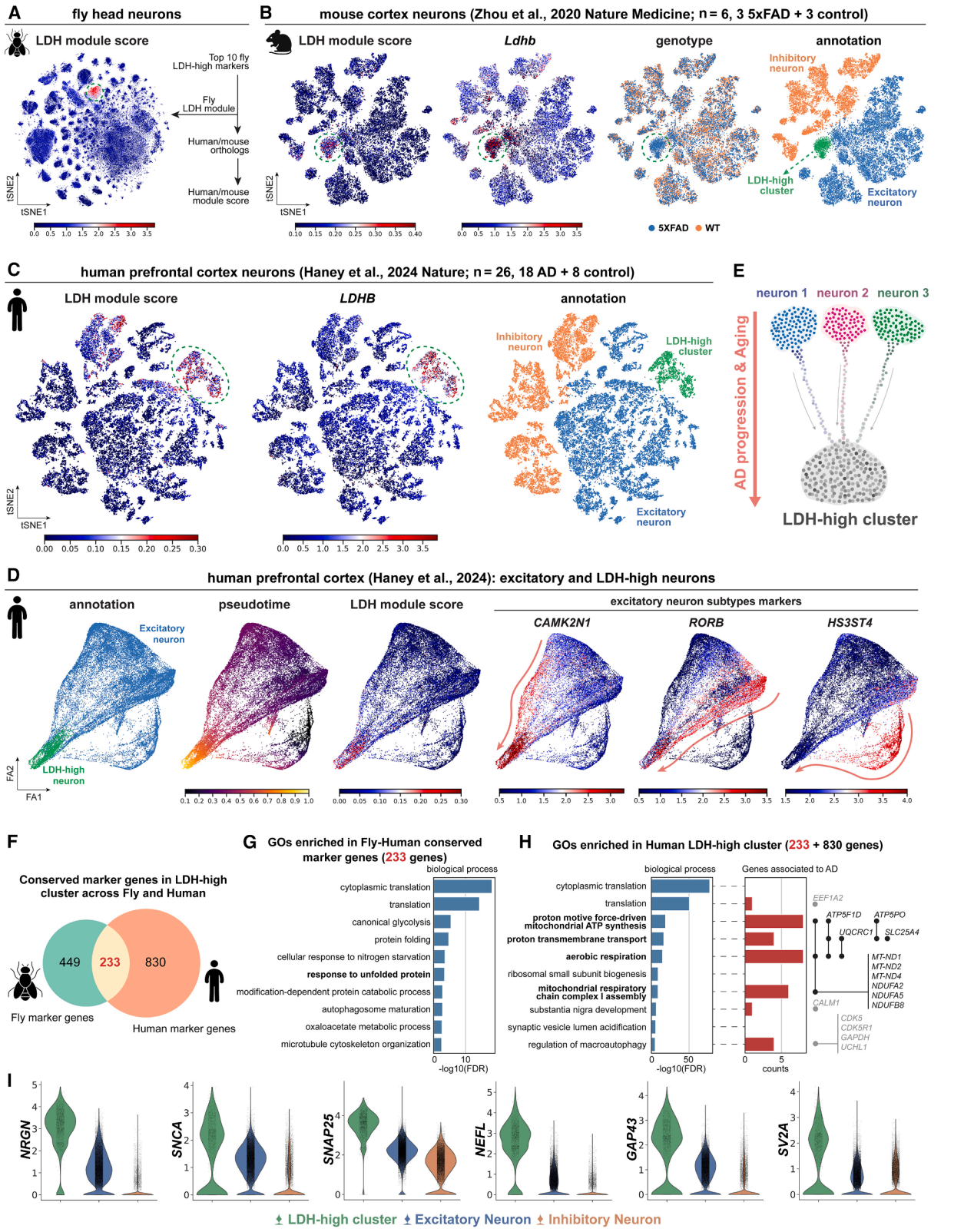

(legend on next page)

Please cite this article in press as: Park et al., Distinct systemic impacts of Aβ42 and Tau revealed by whole-organism snRNA-seq, Neuron (2025), https://doi.org/10.1016/j.neuron.2025.04.017

in AD.[49] Interestingly, this cluster shows enrichment of genes whose proteins have been used as indicators for neurodegeneration in blood plasma or cerebrospinal fluid[50] (Figures 4I and S9B), suggesting that the transcriptional upregulation of these genes may also serve as indicators for neurodegeneration.

Neuronal expression of hTau induces various changes in peripheral tissues

To characterize how neuronal expression of Aβ42 or hTau impacts peripheral tissues, we next focused on the data from fly bodies (Figures 5A and 5B). We found that hTau flies show more obvious peripheral changes than Aβ42 flies. To quantify those changes, we measured differences in the number of DEGs and nuclear ratio between hTau and control flies (Figures 5C, S10A, and S10B). Indeed, cell types within these tissues displayed divergent transcriptomes and cell compositions. Functionally, these top impacted peripheral cell types fall into three categories: fat metabolism, digestion, and reproduction (Figure 5C).

The fly fat body is a central storage depot of nutrients and energy reserves and shares functional similarities with the mammalian adipose tissue, liver, and immune system.[51,52] To assess potential defects in lipid metabolism within this tissue, we dissected and stained the fat body with Nile red to visualize lipid droplets (LDs). In early-stage (20-day) hTau flies, we observed a significant increase in LD size compared with age-matched control flies (Figure 5D). By contrast, we observed smaller and more fragmented LDs in late-stage (30-day) hTau flies (Figure 5D). We next performed Kyoto Encyclopedia of Genes and Genomes (KEGG) pathway enrichment analysis (Figures S10C and S10D) and identified fatty acid degradation as a significantly suppressed pathway (Figure S10C), suggesting that impaired lipid degradation may contribute to LD enlargement in early-stage hTau flies. In the late stage, however, LDs become smaller and more fragmented, likely due to further reductions in fatty acid elongation and biosynthesis pathways (Figure S10E). These findings suggest a progressive and dynamic dysregulation of lipid metabolism in hTau flies.

To assess if lipid metabolism is similarly affected in mammals, we measured adipocyte size, which correlates with the size of LDs,[53] in the inguinal white adipose tissue (iWAT) and epididymal white adipose tissue (eWAT) from PS19 mice, a tauopathy model.[54] These mice have a median lifespan of around 9 months, with about 80% dying by 12 months.[55] Like our early-stage hTau fly data (Figure 5D), 5-month-old PS19 mice show a trend of increased adipocyte size in eWAT, though not statistically significant ($p = 0.0549$) (Figure S10F). By contrast, 9-month-old PS19 mice exhibit a significant reduction in adipocyte size in both iWAT and eWAT compared with age-matched controls (Figure S10F), consistent with our late-stage hTau fly data (Figure 5D). Hence, we found that a conserved defect in LD metabolism occurs in adipose tissue from both fly and mouse tauopathy models.

We next investigated hTau-associated changes in the fly gut. The *Drosophila* gut epithelium is maintained and regenerated by intestinal stem cells (ISCs) through proliferation and differentiation.[56,57] Aging and different stresses can cause gut dysplasia,[58] in which ISCs become hyperproliferative, and their daughter cells, enteroblasts (EBs), cannot properly differentiate into mature enterocytes (ECs), leading to the accumulation of ISCs and EBs with a decrease in mature ECs (Figure 5E). In a pseudotime analysis, we observed that hTau flies have a reduction of mature ECs and an increase of differentiating ECs (Figure 5F). We also observed gut dysplasia-related phenotypes in hTau fly guts (Figures 5G and S10G–S10I).[59–61] Hence, neuronal expression of hTau disrupts gut homeostasis. In addition, we noted that hTau male flies showed reduced fecundity compared with control male flies (Figure S10J).

Neuronal expression of hTau induces accelerated aging in peripheral tissues

Interestingly, the observed changes in the periphery of hTau flies—defects in lipid metabolism, gut dysplasia, and reduced fecundity—are all associated with aging.[62–64] Hence, we hypothesized that neuronal expression of hTau may accelerate aging in peripheral tissues.

A reliable marker of fly aging identified in our previous AFCA is a progressive change in total transcripts per cell, measured as the number of unique molecular identifiers (UMIs).[16] Hence, we compared the distribution of UMIs from the seven available conditions—three time points for control flies, two time points for Aβ42 flies, and two time points for hTau flies—within fat body cells, follicle main body cells, ECs from the gut, and hemocytes (Figure 6A). We observed that these cell types from 20-day hTau flies had a distribution of UMIs similar to 30-day control flies. By contrast, both 10- and 20-day Aβ42 flies showed a similar pattern to the age-matched controls. Consistently, gene expression level analysis also showed that 20-day hTau flies mimic 30-day control flies (Figure 6B).

Figure 4. Identification and characterization of the LDH-high cluster in mouse 5XFAD model and human AD samples

(A) LDH-module score in fly head neurons with the LDH-high cluster circled.

(B) tSNE plots showing LDH-module score, expression of *Ldh* ortholog (*Ldhb*), genotype, and cell-type annotation in mouse cortex neurons.[40]

(C) tSNE plots showing LDH-module score, expression of *Ldh* ortholog (*LDHB*), and cell-type annotation in human prefrontal cortex neurons.[41]

(D) Trajectory plots showing annotation, pseudotime, LDH-module score, and different excitatory neuron subtype markers (*CAMK2N1*, *RORB*, and *HS3ST4*) in excitatory and LDH-high neurons from the human prefrontal cortex dataset.

(E) Illustration of the LDH-high cluster formation. Neurons from different subtypes undergo transcriptional convergence during aging and AD progression, leading to the formation of the LDH-high cluster.

(F) Venn diagram showing 233 conserved marker genes in LDH-high clusters.

(G) GO enrichment analysis of 233 conserved marker genes.

(H) GO enrichment analysis of human LDH-high cluster marker genes (233 + 830 genes) with key biological processes and AD-associated genes related to each term.

(I) Violin plots displaying the expression levels of genes highly enriched in the LDH-high cluster.

Please cite this article in press as: Park et al., Distinct systemic impacts of Aβ42 and Tau revealed by whole-organism snRNA-seq, Neuron (2025), https://doi.org/10.1016/j.neuron.2025.04.017

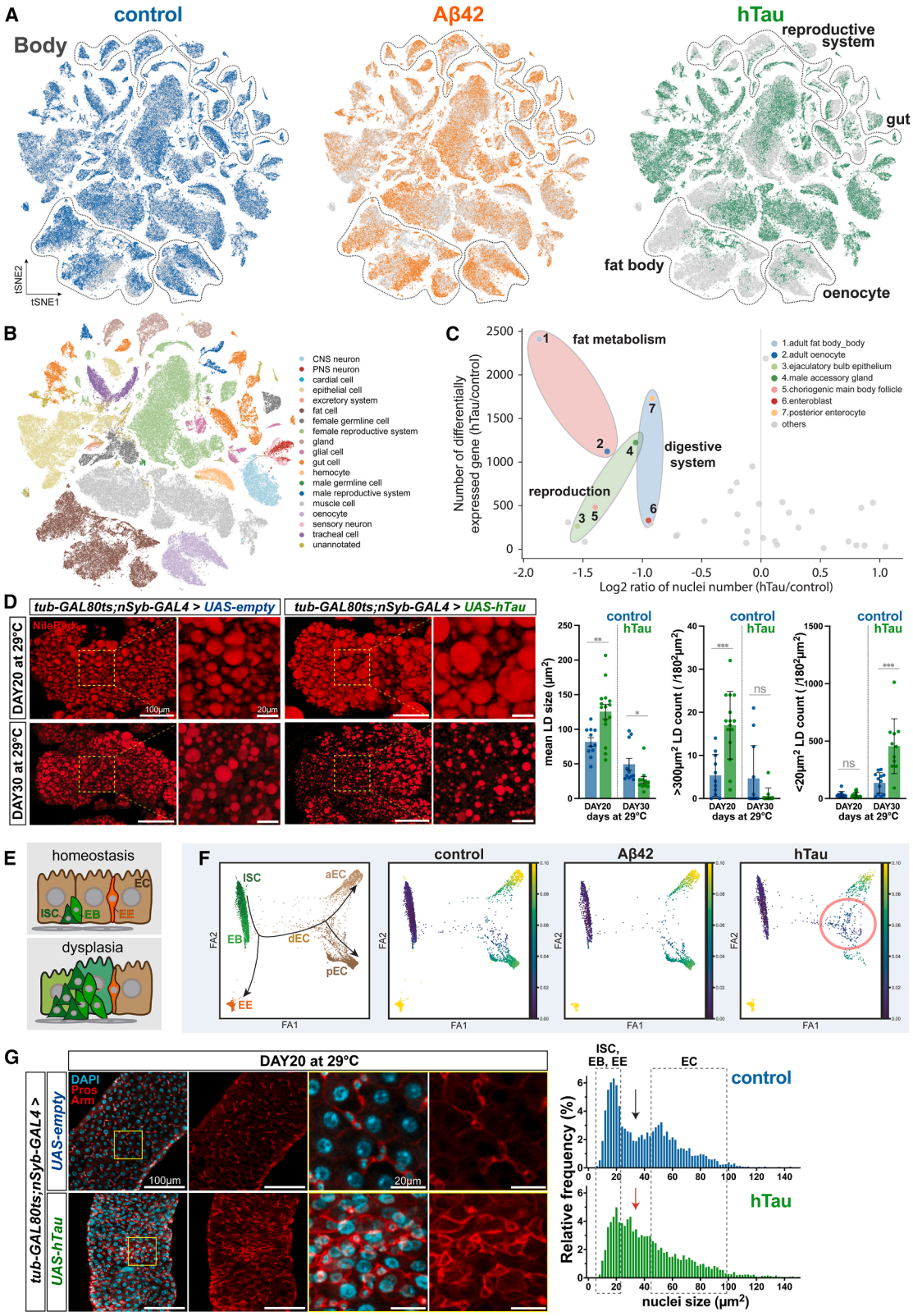

(legend on next page)

Please cite this article in press as: Park et al., Distinct systemic impacts of Aβ42 and Tau revealed by whole-organism snRNA-seq, Neuron (2025), https://doi.org/10.1016/j.neuron.2025.04.017

We further extended our analysis to additional cell types and observed that age-induced changes (30-day control compared with 20-day control) and hTau-induced changes (20-day hTau compared with 20-day control) are highly correlated for both transcript numbers and nuclear ratios (Figures 6C–6F). Changes in the transcript number are not due to differences in the sequencing depth (Figure S1I). Altogether, our data suggest that hTau expression has a broad impact on peripheral tissues and induces an accelerated aging phenotype.

Potential mechanisms underlying peripheral changes in hTau flies

To explore the potential mechanisms underlying hTau-induced aging phenotypes in peripheral tissues, we conducted a comprehensive analysis of brain-body communication using a modified FlyPhoneDB-based cell-cell communication (CCC) analysis[65] (Figure S11A; Table S4). This analysis revealed that hTau flies exhibited 4,725 CCCs that significantly deviated from control flies (Figure S11B). The top ten peripheral cell types with the most differential CCCs include eight cell types that belong to fat metabolism tissues, the digestive system, and the reproductive system (Figures S11C and S11D). This finding is consistent with our earlier analyses showing significant alterations in these three peripheral systems in hTau flies (Figure 5). At the molecular level, we identified several ligand-receptor pairs with prevalent changes (Figure S11E). For example, *cadherin-N2* (*CadN2*), normally expressed in neurons, is broadly upregulated in many peripheral cells of hTau flies (Figure S11F). These results suggest that neuronal hTau may disrupt brain-body communications, contributing to functional changes in peripheral tissues.

In addition, we performed GO analysis on upregulated DEGs in hTau neurons for intrinsic changes. Among the top 50 GO terms, 18 terms are related to synapse organization and axon/dendrite guidance, and 6 terms are associated with synaptic transmission, indicating the impacts of hTau on neuronal structure and synaptic remodeling/function (Figure S11G). Our immunostaining of enteric neurons innervating the hindgut revealed a significant increase in synaptic bouton number in hTau flies (Figure S11H). This suggests that changes in neuronal connectivity may influence peripheral tissue through direct interactions, in addition to alterations in brain-body communications through ligand-receptor interactions.

DISCUSSION

The AD-FCA presents a comprehensive resource for data mining, focusing on how neuronally expressed AD-associated proteins, Aβ42 or Tau, impact neurons and peripheral tissues using *Drosophila*. Our analysis unveiled an unexpected vulnerability of sensory systems to Aβ42 and discovered a conserved LDH-high cluster. For hTau, we found that widespread peripheral tissue disruptions are caused by neuronal hTau expression, resembling an accelerated aging phenotype. Overall, our AD-FCA offers new perspectives into how Aβ42 or hTau systemically affects a whole organism, paving the way for the identification of novel biomarkers and promoting our understanding of brain-body communication in neurodegeneration.

Distinct and shared impacts caused by Aβ42 or hTau

We found that despite both Aβ42 and hTau being toxic, the consequences are significantly different between the two models. While neuronal Aβ42 primarily impacts neurons, neuronal hTau induces accelerated aging in the periphery. Note that differences in neuronal death and dysfunction caused by Aβ42 versus hTau expression have been documented in the fly eye.[20] In human AD, both Aβ42 and Tau accumulate while Aβ42 plaques form prior to neurofibrillary tangles, and each pathology is enriched in distinct brain regions.[66] Although Aβ42 and hTau exhibit distinct systemic effects, they also share noteworthy commonalities (Figures S12A–S12C; Table S3), highlighting potential core mechanisms underlying neurodegeneration. Notably, we observed an enrichment of calmodulin-related genes in both Aβ42 and hTau fly neurons, suggesting a common mechanism where the two pathologies may overlap.[67] In addition, *cindr* (orthologous to human *CD2AP*) and *Snap25* emerged as commonly dysregulated genes. These genes have been previously implicated in AD etiology or identified as an AD biomarker.[10,68,69] Overall, our findings offer novel insights into how Aβ42 and Tau may synergistically and separately contribute to disease progression.

Cell-type vulnerability in AD and in response to Aβ42

In AD, cell vulnerability refers to the susceptibility of certain cell types, particularly neurons, to damage, dysfunction, and eventually degeneration. Studying cell vulnerability in AD is important to understand disease progression, reveal biomarkers, and identify therapeutic targets. Several recent studies have employed

Figure 5. Systemic effects of neuronal hTau expression on peripheral tissues

(A) tSNE plots of body samples colored by genotypes. Clusters showing obvious changes in the hTau flies are indicated.

(B) tSNE plot of body samples showing broad cell classes.

(C) Cell types with significant changes between hTau and control flies regarding DEG number and nuclear ratios.

(D) Nile red staining to visualize LDs in the fat body. 20-day control (n = 11), 20-day hTau (n = 15), 30-day control (n = 11), and 30-day hTau (n = 11). Scatterplots with bars show mean LD size (mean ± SEM), >300 μm^2 LD count (mean ± SD), and <20 μm^2 LD count (mean ± SD). $^*p \leq 0.05$, $^{**}p \leq 0.01$, $^{***}p \leq 0.001$. p values were computed using the parametric unpaired t test.

(E) Illustration of the dysplasia phenotype in the fly gut. ISC, intestinal stem cell; EB, enteroblast; EE, enteroendocrine cell; EC, enterocyte.

(F) Pseudotime analysis of fly gut cell types from different genotypes. Outlined on the right plot is a group of cells between EBs and mature ECs. aEC, anterior EC; pEC, posterior EC; dEC, differentiating EC.

(G) Reduced abundance of mature polyploid ECs and increased ISC/EB-like cells in 20-day hTau fly guts. Right panels show nuclear size distributions. ISCs, EBs, and EEs are diploid cells with small nuclei, and mature ECs are polyploidy cells with big nuclei. DAPI (cyan), anti-Prospero (red signals in nuclei, EEs), and anti-armadillo (red signals in cell membrane, stronger in ISCs and EBs than ECs). Control (n = 12), hTau (n = 16).

For (D) and (G), representative images were generated by the MAX intensity of all Z planes.

Please cite this article in press as: Park et al., Distinct systemic impacts of Aβ42 and Tau revealed by whole-organism snRNA-seq, Neuron (2025), https://doi.org/10.1016/j.neuron.2025.04.017

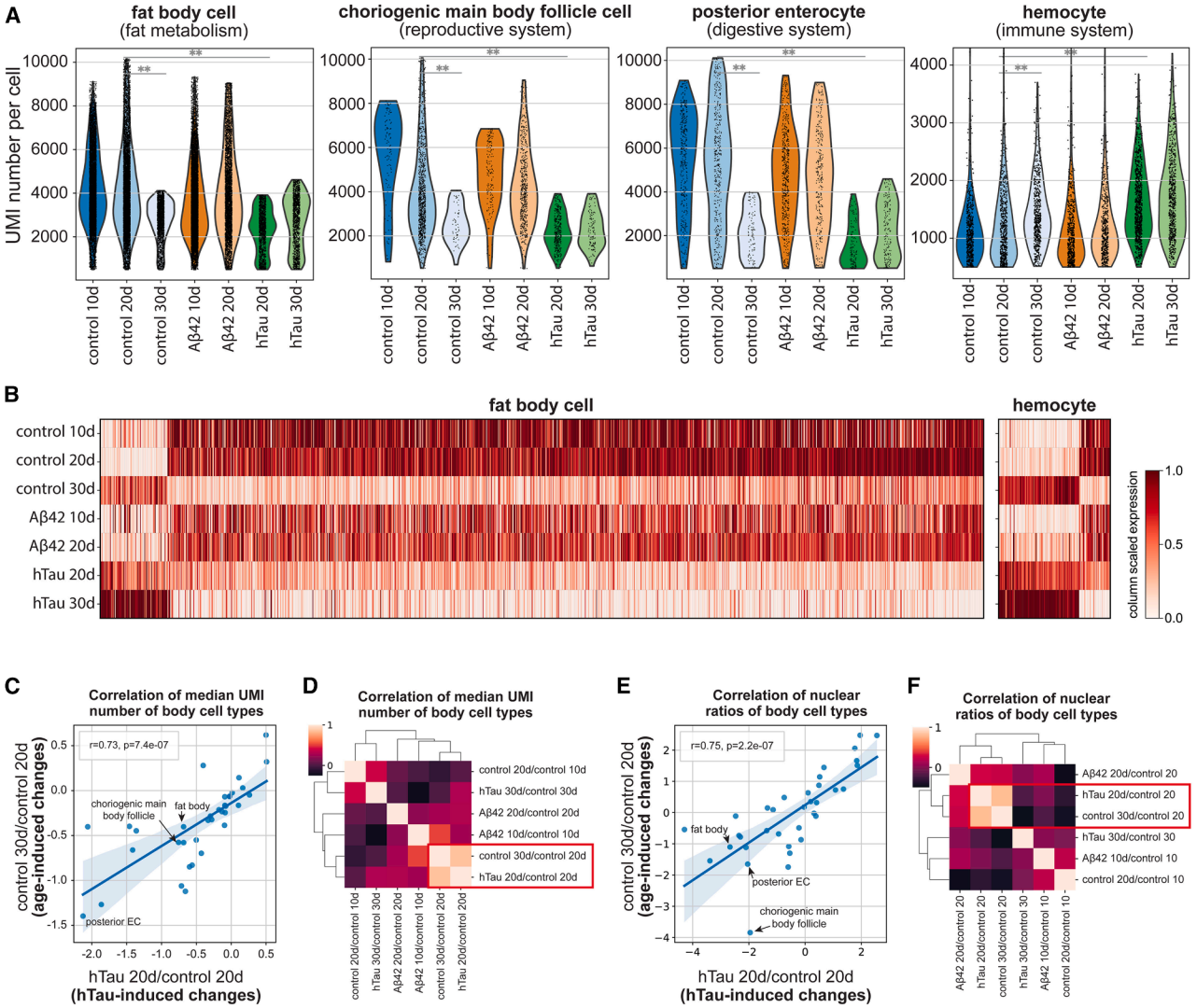

Figure 6. Accelerated aging in hTau flies

(A) Comparison of the number of transcripts per cell (measured by the UMIs). **: Kolmogorov-Smirnov test, false discovery rate < 1e−20. UMI, unique molecular identifier.

(B) Heatmaps showing gene expression patterns in fat body and hemocyte.

(C) Pearson correlation of median UMI numbers between age-induced changes and hTau-induced changes across different cell types.

(D) Spearman correlation of median UMI comparisons between different genotypes and ages. Two comparisons showing the highest correlation are indicated.

(E) Pearson correlation of nuclear ratios between age-induced changes and hTau-induced changes at 20 days across different cell types.

(F) Spearman correlation of nuclear ratios between different genotypes and ages. Two comparisons showing the highest correlation are indicated.

snRNA-seq to study cell vulnerability in different AD models and human AD tissue.[19,42,70–73] Due to the complexity of mammalian systems, most of these studies have focused on a specific brain region and identified specific cell types that are selectively vulnerable. To circumvent this limitation, we used *Drosophila*, as it provides the opportunity to perform whole-organism snRNA-seq to comprehensively compare CNS neurons, PNS neurons, and additional peripheral cell types, a goal that is not easily attainable in mammals.

Our data show that sensory neurons, including ORNs, are among the top impacted cell types in Aβ42 flies (see Figure 2). A decline in olfaction is a common feature of AD.[27,74] However, olfactory dysfunction is frequently overlooked by both physicians and patients due to three major challenges. First, aging can also cause olfactory decline, and it is difficult to distinguish age- versus AD-associated olfactory decline. Second, there are many types of ORNs (about 800 in humans), and it is difficult to assess which ORNs are specifically disrupted. Third, the olfactory neural circuit contains ORNs and downstream neurons, and it is largely unknown which neurons are primarily affected. Our current data provide an opportunity to address these questions. Based on cell loss and DEG analysis, we showed that

Please cite this article in press as: Park et al., Distinct systemic impacts of Aβ42 and Tau revealed by whole-organism snRNA-seq, Neuron (2025), https://doi.org/10.1016/j.neuron.2025.04.017

ORNs are more affected than downstream OPNs in response to Aβ42. Our functional data demonstrate that ORN loss is caused by Aβ42 expression more so than by aging (Figures 2H and 2I), consistent with growing literature arguing that olfaction decline is an early feature of AD.[27]

Conservation of the LDH-high cluster

The findings that Aβ42 flies, 5XFAD mice, and AD post-mortem tissue all have an LDH-high neuronal cluster highlight how the fly data can be used to identify conserved molecular mechanisms that impact human disease. In AD tissues, Aβ42 toxicity may promote transcriptional changes within healthy neurons, driving them into the LDH-high cluster. Supporting this, one previous study on AD patient-derived induced neurons (iNs) showed these cells have increased *LDHA* expression compared with iNs derived from age-matched controls.[75] Moreover, our previous work has shown that neuronal lactate-pyruvate interconversion via fly *Ldh* contributes to glial LD accumulation, a process associated with neurodegeneration.[76] In summary, our investigations into the LDH-high cluster reveal how proper data mining of our AD-FCA can be used to define new avenues for future research.

Aβ42-induced ER stress

ER stress is a highly conserved, protective cellular response to the accumulation of unfolded or misfolded proteins. However, unresolved or prolonged ER stress disrupts cellular homeostasis, can contribute to cell death, and has been implicated in neurodegenerative diseases.[36,37,77] Both our snRNA-seq data and our *in vivo* functional data provide compelling evidence that the ER stress response is activated in most types of neurons in the Aβ42 brain (Figures 3 and S7). We also found that many Ldh-GFP-positive cells in Aβ42 brains exhibit BiP signals (Figure S7I). Previous research documented that downregulation of *ATF4*-dependent ER stress signaling prevents *Ldh* upregulation in flies expressing Aβ42,[78] further supporting that the LDH cluster is associated with ER stress in Aβ42 flies. In addition, many cells exhibiting strong ER stress (BiP positive) in Aβ42 brains were also positive for the apoptosis marker cleaved caspase-3 (Figure S7I). While these findings suggest a potential link between Aβ42-induced ER stress and neuronal death, the relationship appears to be more complex. Notably, a subset of BiP-positive cells does not exhibit strong cleaved caspase-3 signals, indicating that ER stress alone may not be sufficient to drive cell death in all cases or that ER stress precedes cell death. Ultimately, additional factors such as metabolic state, cellular context, or the duration of stress may influence whether ER-stressed neurons undergo apoptosis. Overall, our findings suggest that Aβ42-induced ER stress contributes to neuronal vulnerability, but further investigations are needed to determine the precise mechanisms.

Peripheral aging phenotypes induced by neuronal expression of hTau

We found that hTau induces significant changes in peripheral cells (Figure 5). Similar changes have recently been reported in both AD mouse models and patients. For instance, neuronal hTau expression in mice induces gut degeneration.[79] Additionally, an age-related decline in sex steroid hormones is a risk factor for AD.[80,81] Our findings that fat metabolism is altered by neuronal expression of hTau are consistent with emerging evidence that adipose metabolism and neurodegeneration may be connected in AD. Indeed, the activity of brown adipose tissue in the body was suggested to influence the development of AD.[82] Our study documents conserved LD defects within adipose tissue in hTau flies and PS19 mice, suggesting that disruptions to peripheral adipose tissue may occur in patients after prominent Tau accumulations. Thus, our AD-FCA offers the possibility for delineating uncharted, conserved peripheral alterations in flies and mammals, with relevance to AD.

AD-FCA: A resource for studying AD-associated mechanisms

The AD-FCA serves as a publicly available resource to promote investigations into the brain-body axis. We present *in vivo* functional data for several tissues as proof of concept. Other scRNA-seq datasets from dissected brains of mutant tauopathy flies have recently been reported,[71,73] which will complement our findings. Indeed, we observed overlapping gene expression features, indicating shared pathogenic mechanisms across tauopathy models, despite differences in experimental design (Figures S12D and S12E). As neuron-glia communication is increasingly highlighted as disrupted in AD,[8,10,41,76,83,84] our AD-FCA can help define differential impacts on neuronal and glial subtypes. Furthermore, the field of brain-body communication has rapidly expanded, with much of the research focusing on specific cellular interactions, including the gut-brain axis, while now broadening to examine other brain-peripheral connections.[85–89] The inclusion of peripheral tissues in our AD-FCA, including PNS and non-neuronal cells, will advance our understanding of brain-body communication and may help identify early disease biomarkers.

Limitations of the study

First, while *Drosophila* models provide valuable insights, they do not recapitulate the complexity of AD. Hence, some findings may not directly translate to human neurodegenerative processes. Second, this study focuses on transgenic models overexpressing human Aβ42 or Tau in adult neurons. These models create robust toxic conditions and are unlikely to fully mimic the natural progression of AD in humans, where neuropathology develops over many decades. Third, although whole-organism snRNA-seq provides a comprehensive transcriptomic dataset, it lacks protein-level information critical in AD. Fourth, while the study identifies differential impacts of Aβ42 and Tau on neuronal and peripheral tissues, the exact mechanisms underlying these observations remain to be elucidated. Addressing these limitations could enhance the translational relevance of our findings from *Drosophila* to human.

RESOURCE AVAILABILITY

Lead contact

Further information and requests for resources and reagents should be directed to and will be fulfilled by the lead contact, Hongjie Li (hongjie.li@bcm.edu).

Materials availability

This study generated snRNA-seq data, which are available as described below, and a generated *UAS-ssp.HA.tag* fly line, which is available upon request.

Data and code availability

Raw FASTQ files, expression matrix, and processed h5ad files, including cell-type annotations, are available at NCBI/GEO (accession number GEO: GSE261656). Codes for data processing and analysis are available at GitHub, archived at Zenodo: https://doi.org/10.5281/zenodo.15205305. All annotated data are also available for visualization, download, and custom analysis at https://hongjielilab.org/adfca.

ACKNOWLEDGMENTS

We thank the Bellen lab and Li lab members for their constructive advice. We thank Drs. Josh Shulman, Benjamin Arenkiel, Hamed Jafar-Nejad, Matthew Moulton, Xiaotong Li, and Jason Karpac for giving feedback; Dr. Jason Tennessen for Ldh fly lines; and Dr. Hermann Steller for the BiP antibody.

T.J. is supported by NIH/NIGMS T32-GM136554. C.-Y.L. and A.-L.H. are supported by an NSTC grant from Taiwan (112-2926-I-A49A-503-G). L.D.G. is supported by the Postdoctoral Fellowship Program in Alzheimer's Disease Research, the BrightFocus Foundation, and the Brain Disorders & Development Training Grant, NINDS T32-NS043124-18. E.O. is supported by UT Health San Antonio IRACDA (NIGMS, K12-GM111726). K.F.B. is supported by the South Texas Alzheimer's Disease Research Center (NIA, P30-AG066546). S.Y. is supported by NIH/NIA RF1-AG071557 and R01-AG071557. Y.Z. is supported by NIH R01-DK136619 and R01-DK136532. H. Z. is supported by NIH P01-AG066606, R01-NS093652, and RF1-Ak020670 and CureAlz Fund. H.J.B. is supported by NIH/NIA R01-AG073260, OD R24-OD02205, OD R24-OD031447, NIH/NIGMS R01-GM067858, NIH/NIA U01-AG072439, the Huffington Foundation, and the endowment of the Chair of the Neurological Research Institute. H.L. is a CPRIT Scholar in Cancer Research (RR200063) and supported by NIH/NIA U01-AG086143, Longevity Impetus Grant, Ted Nash Long Life Foundation, Welch Foundation, and Hevolution/AFAR Foundation.

AUTHOR CONTRIBUTIONS

Conceptualization: Y.-J.P., T.-C.L., H.J.B., and H.L.; snRNA-seq: Y.-J.P. and Y.Q.; computational analysis: Y.-J.P., T.-C.L., and T.J.; fly *in vivo* validation: Y.-J.P., T.J., L.R., C.-Y.L., E.H., C.K., A.-L.H., Y.Q., and H.L.; transgenic fly: S.Y.; mouse adipocyte data: Y.-J.P., X.C., B.W., Y.Z., and H.Z.; human data: T.-C.L., E.O., and K.F.B.; data portal and AD-FCA website: J.C. and H.L.; writing: Y.-J.P., T.-C.L., L.D.G., and H.L.; review and editing: all authors.; supervision: H.J.B. and H.L.; funding acquisition: H.J.B., L.D.G., and H.L.

DECLARATION OF INTERESTS

The authors declare no competing interests.

STAR★METHODS

Detailed methods are provided in the online version of this paper and include the following:

SUPPLEMENTAL INFORMATION

Supplemental information can be found online at https://doi.org/10.1016/j.neuron.2025.04.017.

Received: November 27, 2024
Revised: February 27, 2025
Accepted: April 17, 2025
Published: May 16, 2025

REFERENCES

1. Scheltens, P., Blennow, K., Breteler, M.M.B., de Strooper, B., Frisoni, G. B., Salloway, S., and Van der Flier, W.M. (2016). Alzheimer's disease. Lancet *388*, 505–517. https://doi.org/10.1016/S0140-6736(15)01124-1.
2. Menengiç, K.N., Güngör, F., Ovacık, U., Çınar, N., and Yeldan, İ. (2020). Relation of Respiratory Function and Functional Capacity, Body Composition in Individuals with Alzheimer's Disease. Eur. Respir. J. *56*, 2973. https://doi.org/10.1183/13993003.congress-2020.2973.
3. Stampfer, M.J. (2006). Cardiovascular disease and Alzheimer's disease: common links. J. Intern. Med. *260*, 211–223. https://doi.org/10.1111/j.1365-2796.2006.01687.x.
4. Vogt, N.M., Kerby, R.L., Dill-McFarland, K.A., Harding, S.J., Merluzzi, A. P., Johnson, S.C., Carlsson, C.M., Asthana, S., Zetterberg, H., Blennow, K., et al. (2017). Gut microbiome alterations in Alzheimer's disease. Sci. Rep. *7*, 13537. https://doi.org/10.1038/s41598-017-13601-y.
5. Xiong, J., Kang, S.S., Wang, Z., Liu, X., Kuo, T.-C., Korkmaz, F., Padilla, A., Miyashita, S., Chan, P., Zhang, Z., et al. (2022). FSH blockade improves cognition in mice with Alzheimer's disease. Nature *603*, 470–476. https://doi.org/10.1038/s41586-022-04463-0.
6. Bettcher, B.M., Tansey, M.G., Dorothée, G., and Heneka, M.T. (2021). Peripheral and central immune system crosstalk in Alzheimer disease — a research prospectus. Nat. Rev. Neurol. *17*, 689–701. https://doi.org/10.1038/s41582-021-00549-x.
7. Chan, H.Y., and Bonini, N.M. (2000). Drosophila models of human neurodegenerative disease. Cell Death Differ. *7*, 1075–1080. https://doi.org/10.1038/sj.cdd.4400757.
8. Goodman, L.D., Ralhan, I., Li, X., Lu, S., Moulton, M.J., Park, Y.-J., Zhao, P., Kanca, O., Ghaderpour Taleghani, Z.S.G., Jacquemyn, J., et al. (2024). Tau is required for glial lipid droplet formation and resistance to neuronal oxidative stress. Nat. Neurosci. *27*, 1918–1933. https://doi.org/10.1038/s41593-024-01740-1.

9. McGurk, L., Gomes, E., Guo, L., Mojsilovic-Petrovic, J., Tran, V., Kalb, R. G., Shorter, J., and Bonini, N.M. (2018). Poly(ADP-Ribose) Prevents Pathological Phase Separation of TDP-43 by Promoting Liquid Demixing and Stress Granule Localization. Mol. Cell *71*, 703–717.e9. https://doi.org/10.1016/j.molcel.2018.07.002.

10. Moulton, M.J., Barish, S., Ralhan, I., Chang, J., Goodman, L.D., Harland, J.G., Marcogliese, P.C., Johansson, J.O., Ioannou, M.S., and Bellen, H.J. (2021). Neuronal ROS-induced glial lipid droplet formation is altered by loss of Alzheimer's disease–associated genes. Proc. Natl. Acad. Sci. USA *118*, e2112095118. https://doi.org/10.1073/pnas.2112095118.

11. Piper, M.D.W., and Partridge, L. (2018). *Drosophila* as a model for ageing. Biochim. Biophys. Acta Mol. Basis Dis. *1864*, 2707–2717. https://doi.org/10.1016/j.bbadis.2017.09.016.

12. Tatar, M., Post, S., and Yu, K. (2014). Nutrient control of Drosophila longevity. Trends Endocrinol. Metab. *25*, 509–517. https://doi.org/10.1016/j.tem.2014.02.006.

13. Tabula Muris Consortium (2020). A single-cell transcriptomic atlas characterizes ageing tissues in the mouse. Nature *583*, 590–595. https://doi.org/10.1038/s41586-020-2496-1.

14. Davie, K., Janssens, J., Koldere, D., Waegeneer, M.D., Pech, U., Kreft, Ł., Aibar, S., Makhzami, S., Christiaens, V., González-Blas, C.B., et al. (2018). A Single-Cell Transcriptome Atlas of the Aging Drosophila Brain. Cell *174*, 982–998.e20. https://doi.org/10.1016/j.cell.2018.05.057.

15. Li, H., Janssens, J., De Waegeneer, M., Kolluru, S.S., Davie, K., Gardeux, V., Saelens, W., David, F.P.A., Brbić, M., Spanier, K., et al. (2022). Fly Cell Atlas: A single-nucleus transcriptomic atlas of the adult fruit fly. Science *375*, eabk2432. https://doi.org/10.1126/science.abk2432.

16. Lu, T.-C., Brbić, M., Park, Y.-J., Jackson, T., Chen, J., Kolluru, S.S., Qi, Y., Katheder, N.S., Cai, X.T., Lee, S., et al. (2023). Aging Fly Cell Atlas identifies exhaustive aging features at cellular resolution. Science *380*, eadg0934. https://doi.org/10.1126/science.adg0934.

17. Roux, A.E., Yuan, H., Podshivalova, K., Hendrickson, D., Kerr, R., Kenyon, C., and Kelley, D. (2023). Individual cell types in *C. elegans* age differently and activate distinct cell-protective responses. Cell Rep. *42*, 112902. https://doi.org/10.1016/j.celrep.2023.112902.

18. Siletti, K., Hodge, R., Mossi Albiach, A., Lee, K.W., Ding, S.-L., Hu, L., Lönnerberg, P., Bakken, T., Casper, T., Clark, M., et al. (2023). Transcriptomic diversity of cell types across the adult human brain. Science *382*, eadd7046. https://doi.org/10.1126/science.add7046.

19. Sziraki, A., Lu, Z., Lee, J., Banyai, G., Anderson, S., Abdulraouf, A., Metzner, E., Liao, A., Banfelder, J., Epstein, A., et al. (2023). A global view of aging and Alzheimer's pathogenesis-associated cell population dynamics and molecular signatures in human and mouse brains. Nat. Genet. *55*, 2104–2116. https://doi.org/10.1038/s41588-023-01572-y.

20. Chouhan, A.K., Guo, C., Hsieh, Y.-C., Ye, H., Senturk, M., Zuo, Z., Li, Y., Chatterjee, S., Botas, J., Jackson, G.R., et al. (2016). Uncoupling neuronal death and dysfunction in Drosophila models of neurodegenerative disease. Acta Neuropathol. Commun. *4*, 62. https://doi.org/10.1186/s40478-016-0333-4.

21. Iijima, K., Liu, H.-P., Chiang, A.-S., Hearn, S.A., Konsolaki, M., and Zhong, Y. (2004). Dissecting the pathological effects of human Aβ40 and Aβ42 in Drosophila: A potential model for Alzheimer's disease. Proc. Natl. Acad. Sci. USA *101*, 6623–6628. https://doi.org/10.1073/pnas.0400895101.

22. Prüßing, K., Voigt, A., and Schulz, J.B. (2013). Drosophila melanogaster as a model organism for Alzheimer's disease. Mol. Neurodegener. *8*, 35. https://doi.org/10.1186/1750-1326-8-35.

23. Scheltens, P., De Strooper, B., Kivipelto, M., Holstege, H., Chételat, G., Teunissen, C.E., Cummings, J., and van der Flier, W.M. (2021). Alzheimer's disease. Lancet *397*, 1577–1590. https://doi.org/10.1016/S0140-6736(20)32205-4.

24. Wittmann, C.W., Wszolek, M.F., Shulman, J.M., Salvaterra, P.M., Lewis, J., Hutton, M., and Feany, M.B. (2001). Tauopathy in Drosophila: Neurodegeneration Without Neurofibrillary Tangles. Science *293*, 711–714. https://doi.org/10.1126/science.1062382.

25. Özel, M.N., Simon, F., Jafari, S., Holguera, I., Chen, Y.-C., Benhra, N., El-Danaf, R.N., Kapuralin, K., Malin, J.A., Konstantinides, N., et al. (2021). Neuronal diversity and convergence in a visual system developmental atlas. Nature *589*, 88–95. https://doi.org/10.1038/s41586-020-2879-3.

26. Li, G., and Hidalgo, A. (2020). Adult Neurogenesis in the Drosophila Brain: The Evidence and the Void. Int. J. Mol. Sci. *21*, 6653. https://doi.org/10.3390/ijms21186653.

27. Zou, Y.-M., Lu, D., Liu, L.-P., Zhang, H.-H., and Zhou, Y.-Y. (2016). Olfactory dysfunction in Alzheimer's disease. Neuropsychiatr. Dis. Treat. *12*, 869–875. https://doi.org/10.2147/NDT.S104886.

28. Couto, A., Alenius, M., and Dickson, B.J. (2005). Molecular, Anatomical, and Functional Organization of the Drosophila Olfactory System. Curr. Biol. *15*, 1535–1547. https://doi.org/10.1016/j.cub.2005.07.034.

29. Semmelhack, J.L., and Wang, J.W. (2009). Select Drosophila glomeruli mediate innate olfactory attraction and aversion. Nature *459*, 218–223. https://doi.org/10.1038/nature07983.

30. Suh, G.S.B., Wong, A.M., Hergarden, A.C., Wang, J.W., Simon, A.F., Benzer, S., Axel, R., and Anderson, D.J. (2004). A single population of olfactory sensory neurons mediates an innate avoidance behaviour in Drosophila. Nature *431*, 854–859. https://doi.org/10.1038/nature02980.

31. Jones, W.D., Cayirlioglu, P., Kadow, I.G., and Vosshall, L.B. (2007). Two chemosensory receptors together mediate carbon dioxide detection in Drosophila. Nature *445*, 86–90. https://doi.org/10.1038/nature05466.

32. Pacyna, R.R., Han, S.D., Wroblewski, K.E., McClintock, M.K., and Pinto, J.M. (2023). Rapid olfactory decline during aging predicts dementia and GMV loss in AD brain regions. Alzheimers. Dement. *19*, 1479–1490. https://doi.org/10.1002/alz.12717.

33. Tian, Q., Bilgel, M., Moghekar, A.R., Ferrucci, L., and Resnick, S.M. (2022). Olfaction, Cognitive Impairment, and PET Biomarkers in Community-Dwelling Older Adults. J. Alzheimers Dis. *86*, 1275–1285. https://doi.org/10.3233/JAD-210636.

34. Bawa, S., Brooks, D.S., Neville, K.E., Tipping, M., Sagar, M.A., Kollhoff, J. A., Chawla, G., Geisbrecht, B.V., Tennessen, J.M., Eliceiri, K.W., et al. (2020). Drosophila TRIM32 cooperates with glycolytic enzymes to promote cell growth. eLife *9*, e52358. https://doi.org/10.7554/eLife.52358.

35. Fahrbach, S.E. (2006). STRUCTURE OF THE MUSHROOM BODIES OF THE INSECT BRAIN. Annu. Rev. Entomol. *51*, 209–232. https://doi.org/10.1146/annurev.ento.51.110104.150954.

36. Sano, R., and Reed, J.C. (2013). ER stress-induced cell death mechanisms. Biochim. Biophys. Acta *1833*, 3460–3470. https://doi.org/10.1016/j.bbamcr.2013.06.028.

37. Uddin, M.S., Tewari, D., Sharma, G., Kabir, M.T., Barreto, G.E., Bin-Jumah, M.N., Perveen, A., Abdel-Daim, M.M., and Ashraf, G.M. (2020). Molecular Mechanisms of ER Stress and UPR in the Pathogenesis of Alzheimer's Disease. Mol. Neurobiol. *57*, 2902–2919. https://doi.org/10.1007/s12035-020-01929-y.

38. Osman, R., Tacnet-Delorme, P., Kleman, J.-P., Millet, A., and Frachet, P. (2017). Calreticulin Release at an Early Stage of Death Modulates the Clearance by Macrophages of Apoptotic Cells. Front. Immunol. *8*, 1034. https://doi.org/10.3389/fimmu.2017.01034.

39. Oakley, H., Cole, S.L., Logan, S., Maus, E., Shao, P., Craft, J., Guillozet-Bongaarts, A., Ohno, M., Disterhoft, J., Van Eldik, L., et al. (2006). Intraneuronal beta-amyloid aggregates, neurodegeneration, and neuron loss in transgenic mice with five familial Alzheimer's disease mutations: potential factors in amyloid plaque formation. J. Neurosci. *26*, 10129–10140. https://doi.org/10.1523/JNEUROSCI.1202-06.2006.

40. Zhou, Y., Song, W.M., Andhey, P.S., Swain, A., Levy, T., Miller, K.R., Poliani, P.L., Cominelli, M., Grover, S., Gilfillan, S., et al. (2020). Human and mouse single-nucleus transcriptomics reveal TREM2-dependent and TREM2-independent cellular responses in Alzheimer's disease. Nat. Med. *26*, 131–142. https://doi.org/10.1038/s41591-019-0695-9.

41. Haney, M.S., Pálovics, R., Munson, C.N., Long, C., Johansson, P.K., Yip, O., Dong, W., Rawat, E., West, E., Schlachetzki, J.C.M., et al. (2024). APOE4/4 is linked to damaging lipid droplets in Alzheimer's disease microglia. Nature *628*, 154–161. https://doi.org/10.1038/s41586-024-07185-7.

42. Mathys, H., Peng, Z., Boix, C.A., Victor, M.B., Leary, N., Babu, S., Abdelhady, G., Jiang, X., Ng, A.P., Ghafari, K., et al. (2023). Single-cell atlas reveals correlates of high cognitive function, dementia, and resilience to Alzheimer's disease pathology. Cell *186*, 4365–4385.e27. https://doi.org/10.1016/j.cell.2023.08.039.

43. Hetz, C. (2012). The unfolded protein response: controlling cell fate decisions under ER stress and beyond. Nat. Rev. Mol. Cell Biol. *13*, 89–102. https://doi.org/10.1038/nrm3270.

44. Hetz, C., and Papa, F.R. (2018). The Unfolded Protein Response and Cell Fate Control. Mol. Cell *69*, 169–181. https://doi.org/10.1016/j.molcel.2017.06.017.

45. Armand-Ugon, M., Ansoleaga, B., Berjaoui, S., and Ferrer, I. (2017). Reduced Mitochondrial Activity is Early and Steady in the Entorhinal Cortex but it is Mainly Unmodified in the Frontal Cortex in Alzheimer's Disease. Curr. Alzheimer Res. *14*, 1327–1334. https://doi.org/10.2174/1567205014666170505095921.

46. Li, Y.-J., Oliveira, S.A., Xu, P., Martin, E.R., Stenger, J.E., Scherzer, C.R., Hauser, M.A., Scott, W.K., Small, G.W., Nance, M.A., et al. (2003). Glutathione S-transferase omega-1 modifies age-at-onset of Alzheimer disease and Parkinson disease. Hum. Mol. Genet. *12*, 3259–3267. https://doi.org/10.1093/hmg/ddg357.

47. Ma, S.L., Tang, N.L.S., and Lam, L.C.W. (2016). Association of gene expression and methylation of UQCRC1 to the predisposition of Alzheimer's disease in a Chinese population. J. Psychiatr. Res. *76*, 143–147. https://doi.org/10.1016/j.jpsychires.2016.02.010.

48. Schriml, L.M., Mitraka, E., Munro, J., Tauber, B., Schor, M., Nickle, L., Felix, V., Jeng, L., Bearer, C., Lichenstein, R., et al. (2019). Human Disease Ontology 2018 update: classification, content and workflow expansion. Nucleic Acids Res. *47*, D955–D962. https://doi.org/10.1093/nar/gky1032.

49. Bhatt, S., Puli, L., and Patil, C.R. (2021). Role of reactive oxygen species in the progression of Alzheimer's disease. Drug Discov. Today *26*, 794–803. https://doi.org/10.1016/j.drudis.2020.12.004.

50. Hansson, O. (2021). Biomarkers for neurodegenerative diseases. Nat. Med. *27*, 954–963. https://doi.org/10.1038/s41591-021-01382-x.

51. Chatterjee, N., and Perrimon, N. (2021). What fuels the fly: Energy metabolism in Drosophila and its application to the study of obesity and diabetes. Sci. Adv. *7*, eabg4336. https://doi.org/10.1126/sciadv.abg4336.

52. Harnish, J.M., Link, N., and Yamamoto, S. (2021). Drosophila as a Model for Infectious Diseases. Int. J. Mol. Sci. *22*, 2724. https://doi.org/10.3390/ijms22052724.

53. Konige, M., Wang, H., and Sztalryd, C. (2014). Role of adipose specific lipid droplet proteins in maintaining whole body energy homeostasis. Biochim. Biophys. Acta *1842*, 393–401. https://doi.org/10.1016/j.bbadis.2013.05.007.

54. Yoshiyama, Y., Higuchi, M., Zhang, B., Huang, S.-M., Iwata, N., Saido, T. C., Maeda, J., Suhara, T., Trojanowski, J.Q., and Lee, V.M.-Y. (2007). Synapse Loss and Microglial Activation Precede Tangles in a P301S Tauopathy Mouse Model. Neuron *53*, 337–351. https://doi.org/10.1016/j.neuron.2007.01.010.

55. Zhong, M.Z., Peng, T., Duarte, M.L., Wang, M., and Cai, D. (2024). Updates on mouse models of Alzheimer's disease. Mol. Neurodegener. *19*, 23. https://doi.org/10.1186/s13024-024-00712-0.

56. Micchelli, C.A., and Perrimon, N. (2006). Evidence that stem cells reside in the adult Drosophila midgut epithelium. Nature *439*, 475–479. https://doi.org/10.1038/nature04371.

57. Ohlstein, B., and Spradling, A. (2006). The adult Drosophila posterior midgut is maintained by pluripotent stem cells. Nature *439*, 470–474. https://doi.org/10.1038/nature04333.

58. Li, H., and Jasper, H. (2016). Gastrointestinal stem cells in health and disease: from flies to humans. Dis. Model. Mech. *9*, 487–499. https://doi.org/10.1242/dmm.024232.

59. Holsopple, J.M., Cook, K.R., and Popodi, E.M. (2022). Identification of novel split-GAL4 drivers for the characterization of enteroendocrine cells in the Drosophila melanogaster midgut. G3 (Bethesda) *12*, jkac102. https://doi.org/10.1093/g3journal/jkac102.

60. Holsopple, J.M., Cook, K.R., and Popodi, E.M. (2022). Enteroendocrine cell expression of split-GAL4 drivers bearing regulatory sequences associated with panneuronally expressed genes in Drosophila melanogaster. MicroPublication Biol. *2022*. https://doi.org/10.17912/micropub.biology.000628.

61. Katheder, N.S., Browder, K.C., Chang, D., De Maziere, A., Kujala, P., van Dijk, S., Klumperman, J., Lu, T.-C., Li, H., Lai, Z., et al. (2023). Nicotinic acetylcholine receptor signaling maintains epithelial barrier integrity. eLife *12*, e86381. https://doi.org/10.7554/eLife.86381.

62. Churchill, E.R., Dytham, C., and Thom, M.D.F. (2019). Differing effects of age and starvation on reproductive performance in Drosophila melanogaster. Sci. Rep. *9*, 2167. https://doi.org/10.1038/s41598-019-38843-w.

63. Jasper, H. (2015). Exploring the physiology and pathology of aging in the intestine of Drosophila melanogaster. Invertebr. Reprod. Dev. *59*, 51–58. https://doi.org/10.1080/07924259.2014.963713.

64. Mutlu, A.S., Duffy, J., and Wang, M.C. (2021). Lipid metabolism and lipid signals in aging and longevity. Dev. Cell *56*, 1394–1407. https://doi.org/10.1016/j.devcel.2021.03.034.

65. Liu, Y., Li, J.S.S., Rodiger, J., Comjean, A., Attrill, H., Antonazzo, G., Brown, N.H., Hu, Y., and Perrimon, N. (2022). FlyPhoneDB: an integrated web-based resource for cell–cell communication prediction in Drosophila. Genetics *220*, iyab235. https://doi.org/10.1093/genetics/iyab235.

66. Ito, K., Ahadieh, S., Corrigan, B., French, J., Fullerton, T., and Tensfeldt, T.; Alzheimer's; Disease Working Group (2010). Disease progression meta-analysis model in Alzheimer's disease. Alzheimers Dement. *6*, 39–53. https://doi.org/10.1016/j.jalz.2009.05.665.

67. O'Day, D.H., and Myre, M.A. (2004). Calmodulin-binding domains in Alzheimer's disease proteins: extending the calcium hypothesis. Biochem. Biophys. Res. Commun. *320*, 1051–1054. https://doi.org/10.1016/j.bbrc.2004.06.070.

68. Brinkmalm, A., Brinkmalm, G., Honer, W.G., Frölich, L., Hausner, L., Minthon, L., Hansson, O., Wallin, A., Zetterberg, H., Blennow, K., et al. (2014). SNAP-25 is a promising novel cerebrospinal fluid biomarker for synapse degeneration in Alzheimer's disease. Mol. Neurodegener. *9*, 53. https://doi.org/10.1186/1750-1326-9-53.

69. Ojelade, S.A., Lee, T.V., Giagtzoglou, N., Yu, L., Ugur, B., Li, Y., Duraine, L., Zuo, Z., Petyuk, V., De Jager, P.L.D., et al. (2019). cindr, the Drosophila Homolog of the CD2AP Alzheimer's Disease Risk Gene, Is Required for Synaptic Transmission and Proteostasis. Cell Rep. *28*, 1799–1813.e5. https://doi.org/10.1016/j.celrep.2019.07.041.

70. Lau, S.-F., Cao, H., Fu, A.K.Y., and Ip, N.Y. (2020). Single-nucleus transcriptome analysis reveals dysregulation of angiogenic endothelial cells and neuroprotective glia in Alzheimer's disease. Proc. Natl. Acad. Sci. USA *117*, 25800–25809. https://doi.org/10.1073/pnas.2008762117.

71. Praschberger, R., Kuenen, S., Schoovaerts, N., Kaempf, N., Singh, J., Janssens, J., Swerts, J., Nachman, E., Calatayud, C., Aerts, S., et al. (2023). Neuronal identity defines α-synuclein and tau toxicity. Neuron *111*, 1577–1590.e11. https://doi.org/10.1016/j.neuron.2023.02.033.

72. Wang, B., Martini-Stoica, H., Qi, C., Lu, T.-C., Wang, S., Xiong, W., Qi, Y., Xu, Y., Sardiello, M., Li, H., et al. (2024). TFEB–vacuolar ATPase signaling regulates lysosomal function and microglial activation in tauopathy. Nat. Neurosci. *27*, 48–62. https://doi.org/10.1038/s41593-023-01494-2.

73. Wu, T., Deger, J.M., Ye, H., Guo, C., Dhindsa, J., Pekarek, B.T., Al-Ouran, R., Liu, Z., Al-Ramahi, I., Botas, J., et al. (2023). Tau polarizes an aging transcriptional signature to excitatory neurons and glia. eLife *12*, e85251. https://doi.org/10.7554/eLife.85251.

74. Duff, K., McCaffrey, R.J., and Solomon, G.S. (2002). The Pocket Smell Test: successfully discriminating probable Alzheimer's dementia from vascular dementia and major depression. J. Neuropsychiatry Clin. Neurosci. *14*, 197–201. https://doi.org/10.1176/jnp.14.2.197.

75. Mertens, J., Herdy, J.R., Traxler, L., Schafer, S.T., Schlachetzki, J.C.M., Böhnke, L., Reid, D.A., Lee, H., Zangwill, D., Fernandes, D.P., et al. (2021). Age-dependent instability of mature neuronal fate in induced neurons from Alzheimer's patients. Cell Stem Cell *28*, 1533–1548.e6. https://doi.org/10.1016/j.stem.2021.04.004.

76. Liu, L., MacKenzie, K.R., Putluri, N., Maletić-Savatić, M., and Bellen, H.J. (2017). The Glia-Neuron Lactate Shuttle and Elevated ROS Promote Lipid Synthesis in Neurons and Lipid Droplet Accumulation in Glia via APOE/D. Cell Metab. *26*, 719–737.e6. https://doi.org/10.1016/j.cmet.2017.08.024.

77. Ryoo, H.D. (2015). Drosophila as a model for unfolded protein response research. BMB Rep. *48*, 445–453. https://doi.org/10.5483/BMBRep.2015.48.8.099.

78. Niccoli, T., Kerr, F., Snoeren, I., Fabian, D., Aleyakpo, B., Ivanov, D., Sofola-Adesakin, O., Cryar, A., Adcott, J., Thornton, J., et al. (2021). Activating transcription factor 4-dependent lactate dehydrogenase activation as a protective response to amyloid beta toxicity. Brain Commun. *3*, fcab053. https://doi.org/10.1093/braincomms/fcab053.

79. Xia, Y., Prokop, S., Bell, B.M., Gorion, K.-M.M., Croft, C.L., Nasif, L., Xu, G., Riffe, C.J., Manaois, A.N., Strang, K.H., et al. (2022). Pathogenic tau recruits wild-type tau into brain inclusions and induces gut degeneration in transgenic SPAM mice. Commun. Biol. *5*, 446. https://doi.org/10.1038/s42003-022-03373-1.

80. Moffat, S.D., Zonderman, A.B., Metter, E.J., Kawas, C., Blackman, M.R., Harman, S.M., and Resnick, S.M. (2004). Free testosterone and risk for Alzheimer disease in older men. Neurology *62*, 188–193. https://doi.org/10.1212/WNL.62.2.188.

81. Vest, R.S., and Pike, C.J. (2013). Gender, sex steroid hormones, and Alzheimer's disease. Horm. Behav. *63*, 301–307. https://doi.org/10.1016/j.yhbeh.2012.04.006.

82. Tayanloo-Beik, A., Nikkhah, A., Alaei, S., Goodarzi, P., Rezaei-Tavirani, M., Mafi, A.R., Larijani, B., Shouroki, F.F., and Arjmand, B. (2023). Brown adipose tissue and alzheimer's disease. Metab. Brain Dis. *38*, 91–107. https://doi.org/10.1007/s11011-022-01097-z.

83. Claes, C., Danhash, E.P., Hasselmann, J., Chadarevian, J.P., Shabestari, S.K., England, W.E., Lim, T.E., Hidalgo, J.L.S., Spitale, R.C., Davtyan, H., et al. (2021). Plaque-associated human microglia accumulate lipid droplets in a chimeric model of Alzheimer's disease. Mol. Neurodegener. *16*, 50. https://doi.org/10.1186/s13024-021-00473-0.

84. Liu, L., Zhang, K., Sandoval, H., Yamamoto, S., Jaiswal, M., Sanz, E., Li, Z., Hui, J., Graham, B.H., Quintana, A., et al. (2015). Glial Lipid Droplets and ROS Induced by Mitochondrial Defects Promote Neurodegeneration. Cell *160*, 177–190. https://doi.org/10.1016/j.cell.2014.12.019.

85. Agrawal, N., Lawler, K., Davidson, C.M., Keogh, J.M., Legg, R., INTERVAL, Barroso, I., Farooqi, I.S., and Brand, A.H. (2021). Predicting novel candidate human obesity genes and their site of action by systematic functional screening in Drosophila. PLoS Biol. *19*, e3001255. https://doi.org/10.1371/journal.pbio.3001255.

86. Dus, M., Lai, J.S.Y., Gunapala, K.M., Min, S., Tayler, T.D., Hergarden, A.C., Geraud, E., Joseph, C.M., and Suh, G.S.B. (2015). Nutrient Sensor in the Brain Directs the Action of the Brain-Gut Axis in Drosophila. Neuron *87*, 139–151. https://doi.org/10.1016/j.neuron.2015.05.032.

87. Furlan, A., and Petrus, P. (2023). Brain-body communication in metabolic control. Trends Endocrinol. Metab. *34*, 813–822. https://doi.org/10.1016/j.tem.2023.08.014.

88. Jin, H., Li, M., Jeong, E., Castro-Martinez, F., and Zuker, C.S. (2024). A body-brain circuit that regulates body inflammatory responses. Nature *630*, 695–703. https://doi.org/10.1038/s41586-024-07469-y.

89. Morais, L.H., Schreiber, H.L.t., and Mazmanian, S.K. (2021). The gut microbiota-brain axis in behaviour and brain disorders. Nat. Rev. Microbiol. *19*, 241–255. https://doi.org/10.1038/s41579-020-00460-0.

90. Ryoo, H.D., Domingos, P.M., Kang, M.J., and Steller, H. (2007). Unfolded protein response in a Drosophila model for retinal degeneration. EMBO J. *26*, 242–252. https://doi.org/10.1038/sj.emboj.7601477.

91. Fleming, S.J., Chaffin, M.D., Arduini, A., Akkad, A.-D., Banks, E., Marioni, J.C., Philippakis, A.A., Ellinor, P.T., and Babadi, M. (2023). Unsupervised removal of systematic background noise from droplet-based single-cell experiments using CellBender. Nat. Methods *20*, 1323–1335. https://doi.org/10.1038/s41592-023-01943-7.

92. Germain, P.-L., Lun, A., García Meixide, C., Macnair, W., and Robinson, M.D. (2022). Doublet identification in single-cell sequencing data using *scDblFinder*. F1000Res. *10*, 979. https://doi.org/10.12688/f1000research.73600.2.

93. Wolf, F.A., Angerer, P., and Theis, F.J. (2018). SCANPY: large-scale single-cell gene expression data analysis. Genome Biol. *19*, 15. https://doi.org/10.1186/s13059-017-1382-0.

94. Klopfenstein, D.V., Zhang, L., Pedersen, B.S., Ramírez, F., Warwick Vesztrocy, A., Naldi, A., Mungall, C.J., Yunes, J.M., Botvinnik, O., Weigel, M., et al. (2018). GOATOOLS: A Python library for Gene Ontology analyses. Sci. Rep. *8*, 10872. https://doi.org/10.1038/s41598-018-28948-z.

95. Fang, Z., Liu, X., and Peltz, G. (2023). GSEApy: a comprehensive package for performing gene set enrichment analysis in Python. Bioinformatics *39*, btac757. https://doi.org/10.1093/bioinformatics/btac757.

96. Ouyang, J.F., Kamaraj, U.S., Cao, E.Y., and Rackham, O.J.L. (2021). ShinyCell: simple and sharable visualization of single-cell gene expression data. Bioinformatics *37*, 3374–3376. https://doi.org/10.1093/bioinformatics/btab209.

97. Steinhilb, M.L., Dias-Santagata, D., Fulga, T.A., Felch, D.L., and Feany, M.B. (2007). Tau phosphorylation sites work in concert to promote neurotoxicity in vivo. Mol. Biol. Cell *18*, 5060–5068. https://doi.org/10.1091/mbc.e07-04-0327.

98. Park, Y.-J., Kim, S., Shim, H.-P., Park, J.H., Lee, G., Kim, T.-Y., Jo, M.-C., Kwon, A.-Y., Lee, M., Lee, S., et al. (2021). Phosphatidylserine synthase plays an essential role in glia and affects development, as well as the maintenance of neuronal function. iScience *24*, 102899. https://doi.org/10.1016/j.isci.2021.102899.

99. McLaughlin, C.N., Qi, Y., Quake, S.R., Luo, L., and Li, H. (2022). Isolation and RNA sequencing of single nuclei from *Drosophila* tissues. Star Protoc. *3*, 101417. https://doi.org/10.1016/j.xpro.2022.101417.

100. Korsunsky, I., Millard, N., Fan, J., Slowikowski, K., Zhang, F., Wei, K., Baglaenko, Y., Brenner, M., Loh, P.-R., and Raychaudhuri, S. (2019). Fast, sensitive and accurate integration of single-cell data with Harmony. Nat. Methods *16*, 1289–1296. https://doi.org/10.1038/s41592-019-0619-0.

101. Kanehisa, M., and Goto, S. (2000). KEGG: kyoto encyclopedia of genes and genomes. Nucleic Acids Res. *28*, 27–30. https://doi.org/10.1093/nar/28.1.27.

102. Hu, Y., Flockhart, I., Vinayagam, A., Bergwitz, C., Berger, B., Perrimon, N., and Mohr, S.E. (2011). An integrative approach to ortholog prediction for disease-focused and other functional studies. BMC Bioinformatics *12*, 357. https://doi.org/10.1186/1471-2105-12-357.

103. Palladino, M.J., Hadley, T.J., and Ganetzky, B. (2002). Temperature-Sensitive Paralytic Mutants Are Enriched For Those Causing Neurodegeneration in Drosophila. Genetics *161*, 1197–1208. https://doi.org/10.1093/genetics/161.3.1197.

104. Schlegel, P., Yin, Y., Bates, A.S., Dorkenwald, S., Eichler, K., Brooks, P., Han, D.S., Gkantia, M., Dos Santos, M., Munnelly, E.J., et al. (2024).

Whole-brain annotation and multi-connectome cell typing of Drosophila. Nature *634*, 139–152. https://doi.org/10.1038/s41586-024-07686-5.

105. Yoon, J.G., and Stay, B. (1995). Immunocytochemical localization of Diploptera punctata allatostatin-like peptide in Drosophila melanogaster. J. Comp. Neurol. *363*, 475–488. https://doi.org/10.1002/cne.903630310.

106. Stevens, M., Nanou, A., Terstappen, L.W.M.M., Driemel, C., Stoecklein, N.H., and Coumans, F.A.W. (2022). StarDist Image Segmentation Improves Circulating Tumor Cell Detection. Cancers *14*, 2916. https://doi.org/10.3390/cancers14122916.

107. Sieckmann, K., Winnerling, N., Huebecker, M., Leyendecker, P., Juliana Silva Ribeiro, D., Gnad, T., Pfeifer, A., Wachten, D., and Hansen, J.N. (2022). AdipoQ—a simple, open-source software to quantify adipocyte morphology and function in tissues and in vitro. Mol. Biol. Cell *33*, br22. https://doi.org/10.1091/mbc.E21-11-0592.

108. Brand, A.H., and Perrimon, N. (1993). Targeted gene expression as a means of altering cell fates and generating dominant phenotypes. Development *118*, 401–415. https://doi.org/10.1242/dev.118.2.401.

109. Bischof, J., Maeda, R.K., Hediger, M., Karch, F., and Basler, K. (2007). An optimized transgenesis system for Drosophila using germ-line-specific φC31 integrases. Proc. Natl. Acad. Sci. USA *104*, 3312–3317. https://doi.org/10.1073/pnas.0611511104.

110. Venken, K.J.T., He, Y., Hoskins, R.A., and Bellen, H.J. (2006). P[acman]: A BAC Transgenic Platform for Targeted Insertion of Large DNA Fragments in D. melanogaster. Science *314*, 1747–1751. https://doi.org/10.1126/science.1134426.

Please cite this article in press as: Park et al., Distinct systemic impacts of Aβ42 and Tau revealed by whole-organism snRNA-seq, Neuron (2025), https://doi.org/10.1016/j.neuron.2025.04.017

STAR★METHODS

KEY RESOURCES TABLE

REAGENT or RESOURCE	SOURCE	IDENTIFIER
Antibodies		
mouse anti-Aβ42	BioLegend	#805509; RRID: AB_2783381
mouse anti-hyperphosphorylated-Tau (AT8)	ThermoFisher	#MN1020; RRID: AB_223647
rat anti-NCad	DSHB	DN-Ex #8; RRID: AB_528121
rabbit anti-dsRed(RFP)	Takara	#632496; RRID: AB_10013483
guinea pig anti-BiP(Hsc70-3)	gift from Dr. Hermann Steller; Ryoo et al.[90]	N/A
mouse anti-HA 16B12	BioLegend	#901501; RRID: AB_2565006
rabbit anti-Cleaved Caspase-3	Cell Signaling Technology	#9661; RRID: AB_2341188
mouse anti-Elav	DSHB	9F8A9; RRID: AB_528217
rabbit anti-pH3	Cell Signaling Technology	#9701; RRID: AB_331535
mouse anti-armadillo	DSHB	N2 7A1; RRID: AB_528089
mouse anti-prospero	DSHB	MR1A; RRID: AB_528440
mouse anti-Ast7 (allatostatin)	DSHB	5F10; RRID: AB_528076
Alexa Fluor 647 AffiniPure Donkey Anti-Guinea Pig	Jackson ImmunoResearch	#706-605-148; RRID: AB_2340476
Alexa Fluor 647 AffiniPure Goat Anti-Rat	Jackson ImmunoResearch	#112-605-167; RRID: AB_2338404
Alexa Fluor 488 AffiniPure Donkey Anti-Mouse	Jackson ImmunoResearch	#715-545-151; RRID: AB_2341099
Alexa Fluor 647 AffiniPure Donkey Anti-Mouse	Jackson ImmunoResearch	#715-605-150; RRID: AB_2340862
Cy3 AffiniPure Donkey Anti-Mouse	Jackson ImmunoResearch	#715-165-151; RRID: AB_2315777
Cy3 AffiniPure Donkey Anti-Rabbit	Jackson ImmunoResearch	#711-165-152; RRID: AB_2307443
Chemicals, peptides, and recombinant proteins		
Nile Red	Sigma Aldrich	N3103
RNase inhibitor: RNasin Plus	Promega	N2615
Ethyl alcohol, Pure	Sigma Aldrich	E7023
Chloroform	Fisher Scientific	C298-500
Acetic acid glacial	Fisher Scientific	MAX00739
Paraplast Plus	Sigma Aldrich	P3683
Harris Hematoxylin Solution	Sigma Aldrich	HHS16
Eosin Y solution	Sigma Aldrich	#318906
Xylene	J.T.Baker	1330-20-7
Critical commercial assays		
Chromium Next GEM Single Cell 3' HT(high-throughput) Reagent Kits v3.1 (Dual Index)	10X Genomics	PN-1000348
Chromium Next GEM Chip M Single Cell Kit	10X Genomics	PN-1000371
Dual Index Kit TT Set A	10X Genomics	PN-1000215
Deposited data		
Raw sequencing files and processed data of snRNA-seq	GEO	GEO: GSE261656
AD-FCA website	This study	https://hongjielilab.org/adfca/
Experimental models: Organisms/strains		
Drosophila: *tub-GAL80^{ts}*: *w*;P{tubP-GAL80ts}10;TM2/TM6B, Tb1*	Bloomington Drosophila Stock Center	BL7108
Drosophila: *nSyb-GAL4*: *y1 w*; P{nSyb-GAL4.S}3*	Bloomington Drosophila Stock Center	BL51635
Drosophila: *UAS-empty*: *w[1118];;UAS-empty/TM6B Tb1*	Moulton et al.[10]	N/A
Drosophila: *UAS-Aβ42 (II)*: *yw;P{UAS-APP.Abeta42.B}m26a (II)*	Chouhan et al.[20]	N/A

(*Continued on next page*)

Please cite this article in press as: Park et al., Distinct systemic impacts of Aβ42 and Tau revealed by whole-organism snRNA-seq, Neuron (2025), https://doi.org/10.1016/j.neuron.2025.04.017

Continued

REAGENT or RESOURCE	SOURCE	IDENTIFIER
Drosophila: *UAS-Aβ42 (III)*: *yw; P{UAS-APP.Abeta42.B}m17a (III)*	Chouhan et al.[20]	N/A
Drosophila: *UAS-hTau*: *w[1118]; UAS-humanTau^{0N4R}/TM3, Sb[1]*	Wittmann et al.[24]	N/A
Drosophila: *UAS-ssp.3XHA (II)*	This study	N/A
Drosophila: *Gr21a:syt-RFP (III)*	Jones et al.[31]	N/A
Drosophila: *Ldh-GFP*: *w*; P{Ldh-optGFP}attP40*	Bloomington Drosophila Stock Center	BL94704
Mouse: *B6;C3-Tg(Prnp-MAPT*P301S)PS19Vle/J*	The Jackson Laboratory	008169, RRID:IMSR_JAX:008169
Mouse: *B6C3F1/J*	The Jackson Laboratory	100010, RRID:IMSR_JAX:100010
Software and algorithms		
Cell Ranger 6.1.2	10X Genomics	https://www.10xgenomics.com/support/software/cell-ranger/
CellBender 0.2.2	Fleming et al.[91]	https://github.com/broadinstitute/CellBender
scDblFinder 1.8.0	Germain et al.[92]	https://bioconductor.org/packages/release/bioc/html/scDblFinder.html
Scanpy 1.8.2	Wolf et al.[93]	https://scanpy.readthedocs.io/en/stable/
GOATOOLS 1.2.3	Klopfenstein et al.[94]	https://github.com/tanghaibao/goatools
GSEApy 1.1.2	Fang et al.[95]	https://github.com/zqfang/GSEApy
FlyPhoneDB	Liu et al.[65]	https://github.com/liuyifang/FlyPhoneDB
ShinyCell 2.1.0	Ouyang et al.[96]	https://github.com/SGDDNB/ShinyCell

EXPERIMENTAL MODEL AND STUDY PARTICIPANT DETAILS

Drosophila husbandry, fly lines, and genotypes

Flies were maintained on standard cornmeal-molasses medium with a 12-hour light-dark cycle. *tub-GAL80^{ts}; nSyb-GAL4* virgin flies crossed to *UAS-empty*, *UAS-Aβ42*, or *UAS-hTau* transgenic male flies. Each UAS line was combined with *Gr21a:syt-RFP* or *Ldh-GFP* flies for Gr21a ORN and Ldh related experiments. To avoid developmental expression-caused defects, flies were kept at 18°C during cross and developmental process. Progenies were allowed to mate for the first 1-4 days at 18°C and moved to 29°C to express transgenes in pan-neurons from the adult stage. The *UAS-Aβ42* transgenic line was selected based on its previous characterization as being neurotoxic and that it produces a secreted *Aβ42* peptide.[20] The *UAS-hTau^{0N4R}* transgenic line was selected based on its previous characterization as being neurotoxic and that it produces hyperphosphorylated 4R-Tau protein.[24,97]

The table below details the fly lines used.

Fly lines	Genotype	Source/reference	notes
tub-GAL80^{ts}	*w*;P{tubP-GAL80ts}10;TM2/TM6B, Tb1*	BDSC #7108	
nSyb-GAL4	*y1 w*; P{nSyb-GAL4.S}3*	BDSC #51635	
UAS-empty	*w[1118];;UAS-empty/TM6B, Tb1*	Moulton et al.[10]	pGW vector injected to VK33
UAS-Aβ42 (II)	*yw;P{UAS-APP.Aβ42.B}m26a (II)*	Chouhan et al.[20]	Used for most of the crosses
UAS-Aβ42 (III)	*yw;; P{UAS-APP.Aβ42.B}m17a (III)*	Chouhan et al.[20]	Only used for combining with *Ldh-GFP (II)*
UAS-hTau	*w[1118];; UAS-humanTau^{0N4R}/TM3, Sb[1]*	Wittmann et al.[24]	Isoform 0N4R
UAS-ssp.HA.tag	*UAS-ssp.3xHA (II)*	This study	See STAR Methods
Gr21a:syt-RFP	*Gr21a:syt-RFP (III)*	Jones et al.[31]	
Ldh-GFP	*w*; P{Ldh-optGFP}attP40*	BDSC #94704	

METHOD DETAILS

Sample collection, lifespan, and negative geotaxis assays

Progenies were collected 3 days after the first fly hatched at 18°C. Flies were allowed to mate for 1 more day at 18°C. Then, male and female flies were separated into different cages (150 flies per cage) and incubated at 29°C. Fly food was changed every 2 days. For sample collection, fly heads and bodies were dissected at different time points, 10-day, 20-day, and 30-day (after 29°C incubation started), put into 1.5ml RNase-free Eppendorf tube, flash-frozen using liquid nitrogen, and then stored at –80°C. We put 50 heads or

Please cite this article in press as: Park et al., Distinct systemic impacts of Aβ42 and Tau revealed by whole-organism snRNA-seq, Neuron (2025), https://doi.org/10.1016/j.neuron.2025.04.017

15 bodies in each tube. For longevity assay, dead or censored flies were recorded every 2 days. Female and male flies were counted separately. Survival rates were calculated from the total population. For negative geotaxis assays, we used a climbing kit (used in Park et al.[98]) to compare up to 5 groups at once. 0, 10, 20, or 30-day flies were transferred to an empty vial (20 flies per genotype per set). The climbing kit was gently tapped to force all flies to the bottom and then videotaped for 10 seconds. Flies climbed 5 times per set. Climbing height at 10 seconds was measured by the Tracker software (https://tracker.physlets.org/) for the final data. Female and male flies were separated for this assay. 5 sets of 0-day (n = 100, 40 female and 60 male per genotype), 8 sets of 10-day (n = 160, 80 female and 80 male per genotype), 10 sets of 20-day (n = 200, 100 female and 100 male per genotype), 10 sets of 30-day (n = 200, 100 female and 100 male per genotype). Survival curves and negative geotaxis plots were generated in GraphPad Prism.

Single-nucleus RNA sequencing

Single-nucleus suspensions were prepared following the protocol we described previously.[99] Next, we used the BD AriaIII FACS sorter to collect nuclei. Nuclei were stained by Hoechst-33342 on ice (1:1000; >5min). Hoechst+ nuclei were collected during sorting. Since polyploidy is common for many tissue types in *Drosophila*, we observed different populations of nuclei according to DNA content (Hoechst signal). In order to include all cell populations with different nuclear sizes, we included all nuclear populations from the FACS in samples for single-nucleus RNA sequencing. Individual nuclei were collected into one 1.5ml RNase-free Eppendorf tube with 200μl 1x PBS with 0.5% BSA as the receiving buffer (RNase inhibitor added). For each 10x Genomics run, 200k nuclei were collected. Nuclei were spun down for 10 min at 950g at 4°C, and then resuspended using 80μl or desired amount of 1x PBS with 0.5% BSA (RNase inhibitor added). 2μl of nucleus suspension was used for counting the nuclei with hemocytometers to calculate the concentration. We loaded 50-60K nuclei to the 10x controller to target >20k nuclei for each channel.

Next, we performed snRNA-seq using the 10x Genomics platform with the Chromium Next GEM Single Cell 3' HT (high-throughput) Reagent Kits v3.1 (Dual Index) with the following settings. All PCR reactions were performed using the BioRad C1000 Touch Thermal cycler with a 96-deep Well Reaction Module. The recommended cycle numbers from the 10x protocol were used for cDNA amplification and sample index PCR. As per the 10x protocol, 1:10 dilutions of amplified cDNA and final libraries were evaluated on a bioanalyzer. The final library was sent to Novogene Corporation Inc. for Illumina NovaSeq PE150 S4 lane sequencing with the dual index configuration Read 1 28 cycles, Index 1 (i7) 10 cycles, Index 2 (i5) 10 cycles, and Read 2 90 cycles. A PhiX control library was spiked in at 0.2 to 1% concentration. The sequencing depth is about 30-40K reads per nucleus.

snRNA-seq data processing and clustering

Raw snRNA-seq data, in the form of FASTQ files, underwent alignment to the *Drosophila melanogaster* reference genome (FlyBase release 6.31) using the Cell Ranger software (v6.1.2), employing a pre-mRNA gene transfer format (GTF) file generated by the FCA algorithm.[15] Subsequent steps involved the removal of ambient RNA contamination via CellBender[91] and the identification and exclusion of potential doublet cells using scDblFinder.[92] Quality control criteria necessitated the elimination of cells exhibiting fewer than 200 genes or 500 UMIs. Genes detected in fewer than three nuclei were removed from our analysis. Furthermore, cells with gene or UMI counts exceeding five median absolute deviations from the median were also excluded from the analysis. Additionally, cells harboring over 5% of mitochondrial transcripts were eliminated. The majority of the snRNA-seq data analysis was conducted using the Scanpy package (v1.8.2).[93]

In this study, t-SNE was primarily used to highlight fine-grained clustering of cell populations, given the complexity and large number of cell types in our whole *Drosophila* dataset. While t-SNE excels at preserving local structures and distinguishing distinct clusters for accurate cell type annotation, UMAP is better suited for visualizing both global and local structures. Therefore, in certain cases (e.g., Figures 3G and 3H), we applied UMAP to better capture continuous transitions and identity shifts between clusters, especially where cellular state changes were of primary interest.

Cell-type annotation in AD-FCA

Our approach to annotating cell types in AD-FCA closely mirrored the methodology previously established for AFCA annotations.[16] We integrated AD-FCA samples with existing FCA and AFCA datasets, facilitating their co-clustering. To mitigate batch effects and align dataset variations, the Harmony algorithm[100] was applied to the co-clustered data. Subsequent to adjustment, AFCA-derived cell type labels were assigned to AD-FCA cells using a Logistic Regression classifier, with AFCA serving as the training set and AD-FCA as the test set. These initial automated annotations were subsequently subjected to manual validation and correction to enhance reliability.

To enrich the diversity of cell types identified within our head samples, this annotation strategy was extended to incorporate two additional datasets: FCA antenna data and optical lobe data.[15,25] This integration enabled the identification of additional cell types not present in the original Aging Fly Cell Atlas. Specifically, the optical lobe dataset provided more detailed annotations for neuronal subtypes within the fly's optical system, and the FCA antenna data allowed for refined subcluster annotations of ORNs that were absent in the AFCA dataset. Moreover, we manually annotated the "LDH-high cluster," further contributing to the increased cell type diversity. Through this expanded analysis, we successfully annotated a total of 219 distinct cell types. Note that, although some clusters (e.g., the subclusters within cluster 106 in Figure S2) appear clearly separated based on their transcriptional profiles, many of these unannotated subclusters likely correspond to cell types that have yet to be fully characterized. To avoid potentially misleading classifications, we chose to leave these clusters unannotated.

Please cite this article in press as: Park et al., Distinct systemic impacts of Aβ42 and Tau revealed by whole-organism snRNA-seq, Neuron (2025), https://doi.org/10.1016/j.neuron.2025.04.017

Analysis of cell-composition changes

Quantitative assessments of cell composition changes involved counting cell numbers for each cell type across different ages and genotypes. To calculate the proportion of a given cell type within a specific genotype, the cell count for that cell type and genotype was normalized to the total cell number of the same genotype. This normalization facilitated the comparison of cell type proportions between experimental (Aβ42 or hTau flies) and age-matched control groups. The resulting ratios for the experimental groups were then divided by those of the control groups, with the differences expressed in $\log_2$ scale to quantify relative changes in cell composition. Cell types with more than 700 nuclei were selected for our cell composition analyses.

DEG analysis

To identify genes with altered expression levels in Aβ42 and hTau flies compared to age-matched controls (Figure 1D), we performed DEG analysis using the Wilcoxon Rank Sum test. Genes were considered differentially expressed if they met a false discovery rate (FDR) threshold of <0.05. For DEG analysis, we selected cell types containing more than 700 nuclei, including samples from both male and female flies. To further identify early or late-specific DEGs in Aβ42 flies, we grouped samples by age, incorporating both sexes, and compared them to their respective age-matched controls (Figures S7D and S7E).

To plot Figure 6B, We conducted a comparative analysis of DEGs by evaluating two sets of comparisons. First, we compared the gene expression profiles of 20-day hTau flies to those of 20-day control flies to identify DEGs. Next, we performed a comparison between 30-day control flies and 20-day control flies to obtain a second set of DEGs. Subsequently, we compared the two lists of DEGs to determine the commonly changed genes between the two comparisons.

Gene ontology and pathway enrichment analysis

Differential expression analysis yielded genotype-specific DEGs, encompassing both upregulated and downregulated genes across various cell types. These DEGs were subjected to GO analysis using the GOATOOLS software (v1.2.3).[94] For this purpose, the gene association dataset (FB2019_06) was retrieved from FlyBase, with a specific focus on Biological Process (BP) GO terms for our investigations.

GOs enriched in the human LDH-high cluster were identified using approaches similar to the fly analysis. The human gene association file was downloaded from the GO Consortium website (https://current.geneontology.org/products/pages/downloads.html) and imported into GOATOOLS for identifying enriched GOs.

Pathway enrichment analysis leveraged the Kyoto Encyclopedia of Genes and Genomes (KEGG) database, with *Drosophila*-specific pathways selected to suit our study's requirements.[101] The integration of DEGs with these selected pathways was facilitated through the GSEApy package,[95] enabling the identification of significantly enriched pathways.

Identification of the LDH-high cluster

To delineate marker genes specific to the *Drosophila* LDH-high cluster, we conducted a differential expression analysis by comparing cells within the LDH-high cluster to other neuronal populations in the *Drosophila* dataset. Marker genes were selected based on specific thresholds: an FDR lower than 0.01 and a log fold change greater than 1, indicating notable enrichment in the LDH-high cluster.

To define the LDH-high cluster across species, we first performed an unbiased identification of marker genes in the fly LDH-high cluster and then determined their orthologs in both mice and humans using the DRSC Integrative Ortholog Prediction Tool (DIOPT) version 9.0 with a score threshold of $\geq$5.[102] The top 10 marker genes from flies, which had orthologs in humans and mice, were subsequently used to calculate the LDH module score (Table S2). This was done using the score_genes() function from the Scanpy package. The LDH score for mouse and human neurons was computed based on the expression of genes orthologous to the top 10 fly LDH-high cluster marker genes. Notably, the LDH module scores in mice and humans exhibited lower specificity and enrichment compared to those in flies. This reduced specificity likely results from the expansion of orthologous gene families in mammals, where some orthologs may have diverged in expression patterns relative to their fly counterparts. Additionally, transcriptional rewiring across species may contribute to the observed differences, as certain mouse and human orthologs may not be preferentially expressed in LDH-high neurons. To further validate the conservation of these markers, we manually examined the expression of key genes, including *Ldh* (orthologous to *LDHA* and *LDHB*), *crc* (orthologous to *ATF4*), and cnc (orthologous to *NFE2L1*) (Figures 4, S8, and S9).

Mouse single-nucleus RNA-seq data processing

Gene expression matrices of mouse single-nucleus RNA sequencing data were obtained from the Gene Expression Omnibus (GEO; accession number GSE140511). We followed the same preprocessing pipeline as employed in our fly data analysis, which involved filtering out potential doublets and ambiguous nuclei. Neuronal populations were annotated using well-established markers for excitatory and inhibitory neurons, specifically *Slc17a7* and *Gad1*, respectively. After annotation, neuronal cells were sub-clustered, and the LDH module scores and expression levels of the *Ldha* and *Ldhb* genes, orthologs of the fly *Ldh*, were analyzed to identify the LDH-high cluster in the mouse dataset.

Please cite this article in press as: Park et al., Distinct systemic impacts of Aβ42 and Tau revealed by whole-organism snRNA-seq, Neuron (2025), https://doi.org/10.1016/j.neuron.2025.04.017

CellPress

Human single-nucleus RNA-seq data processing

Processed human single-nucleus RNA sequencing data files in the.h5ad format were obtained for two human Alzheimer's disease datasets from the GEO (accession number GSE254205) and the corresponding author's website at MIT, respectively (https://compbio.mit.edu/ad_aging_brain/).[41,42] First, we reassessed and re-annotated the major cell types within these datasets using the marker genes defined in Haney et al.'s publication. Subsequently, neuronal cell populations were further sub-clustered. Within these sub-clusters, we identified the LDH-high cluster based on the LDH module scores and elevated expression of the human orthologs of fly Ldh, specifically *LDHA* and *LDHB*. Additionally, for comparative analysis, we incorporated a dataset comprising neuronal data from the prefrontal cortex of young, non-AD individuals. This dataset was retrieved from the Human Cell Atlas portal.[18]

Identification of conserved marker genes across species

To identify marker genes of the human LDH-high cluster, we applied the same differential expression strategy used in *Drosophila*, comparing LDH-high neurons to all other neuronal populations. Genes with FDR lower than 0.01 and log fold change larger than 1 were considered significant markers. To evaluate conservation from *Drosophila* to humans, we utilized DIOPT v9.0 to identify human orthologs of all *Drosophila* LDH-high marker genes via the DIOPT API. Genes with a DIOPT score $\geq$ 2 were classified as conserved markers, while genes lacking an identified fly ortholog or those not enriched in the human LDH-high cluster were considered non-conserved.

Convergent trajectory of LDH-high cluster in human AD samples

Trajectory analysis of excitatory neurons and the LDH-high cluster was performed using the partition-based graph abstraction (PAGA) function in Scanpy. To infer the original cell identity of excitatory neurons, we utilized three excitatory neuron subtype markers: *CAMK2N1*, *RORB* and *HS3ST4*. The LDH-high population within this subset was highlighted by computing the LDH score. For pseudotime analysis, excitatory neurons were designated as the root, allowing for the visualization of lineage trajectories and potential shifts toward the LDH-high state in the context of Alzheimer's disease.

Gut snRNA-seq trajectory analysis

Trajectory analysis of the gut cells was performed using Scanpy. The intestinal stem cell lineage was extracted from the data, which included the intestinal stem cells, enteroblasts, adult differentiating enterocytes, enteroendocrine cells, anterior enterocytes of the adult midgut epithelium, and posterior enterocytes of the adult midgut epithelium. The pseudotime of the clusters was inferred using the PAGA function, and then the ForceAtlas2 algorithm was implemented to overlay the cells spatially onto the PAGA plot. To compare the cell compositions of each genotype (control, Aβ42, and hTau), the genotypes were subset separately from the final pseudotime plot.

Correlation analysis of UMI numbers and nuclear ratios

To evaluate the correlation of UMI numbers across cell types, we initially determined the median UMI counts for each cell type within individual samples. These median UMI counts were then compared across various samples to calculate ratios that reflect differences attributable to genotype or age. We utilized Pearson's or Spearman's correlation coefficients to identify groups exhibiting similar trends in UMI number alterations. Furthermore, we extended our correlation analysis to encompass nuclear ratios. These ratios were derived by comparing nuclear counts between pairs of samples, as outlined in the "Analysis of Cell Composition Changes" section. Subsequently, we compared these nuclear ratios across different groups to discern patterns and trends consistent among various comparisons.

Analysis of cell-cell communication

Our investigation into CCC was guided by the foundational principles delineated in FlyPhoneDB, an algorithm that calculates cell-cell interaction scores in *Drosophila* based on ligand-receptor pairs from major signaling pathways[65] with specific adaptations. As some pairs documented in the fly neural system are not included in the FlyPhoneDB database (196 pairs), we expanded the list to include 44 additional pairs based on previous publications and FlyBase annotations. We extracted a collection of genes linked to the GO term "homophilic cell adhesion via plasma membrane adhesion molecules" from FlyBase. This was followed by a manual curation process, resulting in the selection of 44 genes that were subsequently incorporated into the existing ligand-receptor list within the FlyPhoneDB framework (Table S4). Although we refer to these as ''ligand-receptor pairs'', this database consists of both typical ligand-receptor interactions (e.g., *Pvf3-Pvr*, *dpp-tkv*), as well as atypical surface protein-surface protein interactions (e.g., *CadN-CadN*, *Dscam2–Dscam2*), as both can mediate cell-cell interactions.

By querying our snRNA-seq data from both fly heads and whole body, we selected a subset of 102 cell types (all characterized with more than 700 nuclei) and assessed 622,080 possible neuron-to-periphery communications which involve 54 neuronal cell types, 48 peripheral cell types, and 240 ligand-receptor pairs. This facilitated the computation of CCC metrics within each genotype under investigation. Only CCCs exhibiting a p-value less than 0.05 in control or hTau samples were retained for subsequent analyses, ensuring statistical relevance. A total of 93,524 CCC scores (p-value $<$ 0.05) were detected from hTau and control flies, where each score corresponds to one unique ligand-receptor pair, with the ligand originating from neuronal cells and the receptor from peripheral cells. Particular emphasis was placed on CCCs emanating from neurons and targeting peripheral cells, enabling an

Please cite this article in press as: Park et al., Distinct systemic impacts of Aβ42 and Tau revealed by whole-organism snRNA-seq, Neuron (2025), https://doi.org/10.1016/j.neuron.2025.04.017

exploration of the communicative alterations induced by neuronal hTau expression. To quantitatively assess these changes, we computed the 'Delta scores' by subtracting control CCC scores from those of the hTau samples. These Delta scores were then standardized to Z scores based on their corresponding standard deviations. CCCs with absolute Z scores exceeding 2 were classified as differential CCCs, denoting statistically significant communication differences between hTau and control cohorts.

While CCC analysis provides valuable insights, it is also important to acknowledge some limitations, such as potential false positive hits. Further refinement of this analysis, such as incorporating a spatial transcriptome approach, could help address these limitations and provide more accurate results.

AD-FCA data portal website

The AD-FCA web platform was constructed utilizing the Shiny package (version 1.6.0) within the R programming environment (version 4.0.5), facilitating interactive web application development. The platform hosts two principal datasets: the Head dataset and the Body dataset, which encompass snRNA-Seq analytical outcomes derived from head and body tissues, respectively.

For the 'Cell Type' and 'Gene Expression' interface components, data handling and visual representation were executed employing the Tidyverse package (version 1.3.0) and the ggplot2 package (version 3.3.3) in R, ensuring a robust and efficient data processing pipeline. Additionally, the 'Custom Analysis' section of the platform is enriched by the functionalities provided by the ShinyCell package (version 2.1.0),[96] offering users an enhanced and tailored analytical experience.

Comparison of AD-FCA hTau and hTau[P301] fly brain single-cell transcriptome

Brain scRNA-seq data from hTau[P301L] flies[71] were obtained from GEO (accession GSE223626). Neuronal cells were identified based on the original annotations provided by that study. To characterize hTau[P301L]-associated transcriptional changes, we compared neurons from hTau[P301L] flies against neurons from control flies, yielding a set of DEGs specific to hTau[P301L]. These neuronal DEGs were then analyzed using GOATOOLS to determine GO enrichments, and the top 10 GO terms were compared with the top GO terms from our AD-FCA hTau DEGs (Figures S12A and S12D). Additionally, DEGs from the AD-FCA hTau ventral nerve system were compared with the corresponding genes from hTau[P301L] neurons to assess overall transcriptomic similarity (Figure S12E). It is important to note that technical and genetic differences exist among various tauopathy datasets, including the hTau[P301L] model and our AD-FCA hTau flies. These differences should be considered when interpreting and comparing datasets across different studies.

Detection of vacuoles in the brain

To detect vacuoles in the brain, fly heads were fixed in fresh Carnoy's solution (ethanol:chloroform:acetic acid at 6:3:1) at 4°C for at least 24 hours, washed, serially dehydrated with ethanol, and paraffin-embedded using standard histological procedures.[103] Serial 5 μm sections were stained with hematoxylin and eosin and examined under a light microscope. Images were taken with a Nikon NiU Eclipse Upright Microscope.

Whole-brain dissection and immunofluorescence

Fly brains were dissected in 1X PBS using Dumont #55 forceps (FST, 11255-20), placed into 0.2ml PCR strip tubes, and fixed with 4% paraformaldehyde (PFA) in 1X PBS for 20 min at room temperature (RT). The brains were thoroughly washed with 0.3% PBST (1X PBS + 0.3% Triton-X100) and blocked with a brain-blocking buffer (5% normal goat serum (NGS) in 0.3% PBST) for 2 hours at RT. After blocking, the brains were incubated with primary antibodies (see below) in the brain-blocking buffer at 4°C overnight. The brains were thoroughly rinsed with 0.2% PBST and incubated with secondary antibodies (see below) in the brain-blocking buffer at RT for 2 hours. The brains were thoroughly rinsed with 0.3% PBST and 1X PBS, and mounted with SlowFade™ Gold Antifade Mountant (Thermo Fisher, S36936). Images were obtained with Leica STELLARIS 5 confocal microscope as Z series with the same interval. Z series images were merged by ImageJ (Image-Stacks-Z projection-Max Intensity or SUM slices), and then the signal intensity and area were measured using ImageJ. Quantification graphs were generated in GraphPad Prism. P-values were computed using the parametric unpaired t-test. For Ldh-GFP brains, endogenous GFP signal was imaged without antibody staining. Illustrations of brain regions were generated using FlyWire.[104] For Figure 2I, the mean RFP signal intensity/area in the V region was quantified from SUM intensity images by averaging measurements from both sides of the antennal lobes.

Primary antibodies

mouse anti-Aβ42 (1:100, BioLegend, #805509)
mouse anti-hyperphosphorylated-Tau (AT8) (1:500, ThermoFisher, #MN1020)
rat anti-NCad (1:40, DSHB, DN-Ex #8)
rabbit anti-dsRed(RFP) (1:500, Takara, #632496)
guinea pig anti-BiP(Hsc70-3) (1:1000, gift from Dr. Hermann Steller)[90]
mouse anti-HA 16B12 (1:1000, BioLegend, #901501)
rabbit anti-Cleaved Caspase-3 (1:100, Cell Signaling Technology, #9661)

Secondary antibodies (all 1:250 dilution)

Alexa Fluor 647 AffiniPure Donkey Anti-Guinea Pig (Jackson ImmunoResearch, 706-605-148)
Alexa Fluor 647 AffiniPure Goat Anti-Rat (Jackson ImmunoResearch, 112-605-167)

Please cite this article in press as: Park et al., Distinct systemic impacts of Aβ42 and Tau revealed by whole-organism snRNA-seq, Neuron (2025), https://doi.org/10.1016/j.neuron.2025.04.017

Alexa Fluor 488 AffiniPure Donkey Anti-Mouse (Jackson ImmunoResearch, 715-545-151)
Alexa Fluor 647 AffiniPure Donkey Anti-Mouse (Jackson ImmunoResearch, 715-605-150)
Cy3 AffiniPure Donkey Anti-Mouse (Jackson ImmunoResearch, 715-165-151)
Cy3 AffiniPure Donkey Anti-Rabbit (Jackson ImmunoResearch, 711-165-152)

Antenna dissection and imaging

For *Gr21a:syt-RFP* and *Ldh-GFP* antenna, endogenous RFP/GFP signals were imaged without antibody staining. The 2nd and 3rd segments of antenna were dissected together, mounted with SlowFade™ Gold Antifade Mountant, and imaged immediately with Leica STELLARIS 5 confocal microscope as Z series with the same interval. RFP+/GFP+ cell bodies were counted from whole Z planes. Representative images were merged by ImageJ (Image-Stacks-Z projection-Max Intensity). Quantification graphs are generated in GraphPad Prism. P-values were computed using the parametric unpaired t-test.

For auditory sensory neuron nuclei detection, the 2nd and 3rd segments of antenna were dissected together, placed into 0.2ml PCR tubes, and fixed with 4% PFA in 3% PBST (1X PBS + 3% Triton-X100) for 20 min at RT. The antennae were thoroughly washed with 3% PBST and blocked with an antenna-blocking buffer (5% normal goat serum (NGS) in 3% PBST) for 2 hours at RT. After blocking, the brains were incubated with mouse anti-Elav (1:40, DSHB, 9F8A9) in the antenna-blocking buffer at 4°C for 2 days. The antennae were thoroughly rinsed with 3% PBST and incubated with Alexa Fluor 488 AffiniPure Donkey Anti-Mouse (1:250, Jackson ImmunoResearch, 715-545-151) in the antenna blocking buffer at RT for 2 hours. The antennae were thoroughly rinsed with 3% PBST, incubated with DAPI stain (1:1000) for 20 min, washed with 1X PBS, and mounted with SlowFade™ Gold Antifade Mountant (Thermo Fisher, S36936). Images were obtained with Leica STELLARIS 5 confocal microscope as Z series with the same interval. Elav+ cell bodies were counted from whole Z planes. Representative images were merged by ImageJ (Image-Stacks-Z projection-Max Intensity). Quantification graphs were generated in GraphPad Prism. P-values were computed using the parametric unpaired t-test.

Fat body dissection and LD staining

For fat body dissection, fly abdomen filets were dissected in 1X PBS using Vannas Spring Scissors (FST, 3mm Cutting Edge, 15000-00) and forceps. The abdomen filets were placed into 1.5ml Eppendorf tubes, fixed with 4% PFA for 20 min at RT, and washed with 1X PBS. Filets were incubated in Nile Red buffer (1:1,000 dilution of 1 mg/ml Nile Red (Sigma) in 1X PBS) for 10 min at RT, thoroughly rinsed with 1X PBS, and mounted with SlowFade™ Gold Antifade Mountant. Images were obtained with Leica STELLARIS 5 confocal microscope as Z series with the same interval. Z series images were merged by ImageJ (Image-Stacks-Z projection-Max Intensity). The size and number of LD were measured from the same area of each sample by the ImageJ StarDist2D plugin (see StarDist2D quantification).

Gut dissection and immunofluorescence

Fly guts (15-20 females) were dissected in cold 1X PBS, placed into a 24-well plate, and fixed with 4% PFA in 1X PBS for 45 min at RT. The guts were thoroughly washed with 0.2% PBST (1X PBS + 0.2% Triton-X100) and blocked with a gut-blocking buffer (5% normal goat serum (NGS) in 0.2% PBST) for one hour at 4°C. After blocking, the guts were incubated with primary antibodies, rabbit anti-pH3 (1:1000, Cell Signaling Technology, #9701) and a combination cocktail of mouse anti-armadillo (1:100, DSHB, N2 7A1) and mouse anti-prospero (1:250, DSHB, MR1A), in the gut blocking buffer at 4°C overnight. For hindgut enteric neuron staining, we used mouse anti-Ast7 (allatostatin) (1:100, DSHB, 5F10[105]). The guts were thoroughly rinsed with 0.2% PBST and incubated with secondary antibodies, Cy3 AffiniPure Donkey Anti-Rabbit (1:250, Jackson ImmunoResearch, 711-165-152) and Alexa Fluor 647 AffiniPure Donkey Anti-Mouse (Jackson ImmunoResearch, 715-605-150) in gut blocking buffer, at RT for 2 hours. The guts were thoroughly rinsed with 0.2% PBST and incubated with DAPI stain (1:1000) for 20 min at 4°C. The guts were mounted SlowFade™ Gold Antifade Mountant. Images were obtained with Leica STELLARIS 5 confocal microscope as Z series with the same interval. Z series images were merged on half of the Z-stacks (merged = total z-stacks with the gut visible/2) by ImageJ (Image-Stacks-Z projection-Max Intensity), and the DAPI channel was extracted from the image for quantification. The size of each nucleus was measured from the same area of each sample by ImageJ StarDist2D plugin (see StarDist2D quantification).

StarDist2D quantification for LD and gut nuclei

To measure the number and area of fat body LD or gut nuclei for each sample, the ImageJ (Fiji) plugin, StarDist2D, was implemented.[106] Nile Red or DAPI channel was extracted from the images. The StarDist2D plugin parameters were variable between images, but the most accurate settings were applied on a per-image basis. Images were manually curated to remove false positives and add false negatives. The tables of LD/nuclei number and area were produced by the ImageJ measure function. For LD quantification, mean LD size and >300μm^2 LD count were calculated from each sample using Excel. Quantification graphs were generated by GraphPad Prism. P-values were computed using the parametric unpaired t-test. For gut nuclei size quantification, frequency distribution analysis in GraphPad Prism was used (Parameters: Relative frequency percentages. Bin width 2μm^2, Bin each replicate, Bar graph).

Please cite this article in press as: Park et al., Distinct systemic impacts of Aβ42 and Tau revealed by whole-organism snRNA-seq, Neuron (2025), https://doi.org/10.1016/j.neuron.2025.04.017

Male fecundity assay

Individual 20-day male fly (N>25 per genotype, control or hTau flies) was crossed with 3 young wild-type female virgin flies. After mating at 29°C for 3 days, female flies were separated into individual vials (one female/vial) and incubated at 25°C. Fly vials were changed every 3 days. Total numbers of progenies from each cross were counted, including the mating vial, and divided by the number of female flies. Dead flies during mating were censored.

Mouse adipose tissue histology

All protocols involving mice were approved by the Institutional Animal Care and Use Committee of Baylor College of Medicine. PS19 (Tau) mice were obtained from Jackson Labs (008169).[54] Heterozygote PS19 mice were bred to B6C3F1/J wild-type mice to maintain the line. 5-month-old and 9-month-old heterozygote PS19 male mice were used and compared to wild-type male siblings for adipose tissue histology. After the mice were euthanized, the tissue was immediately excised, fixed overnight in 10% PBS-buffered formalin, and then stored in 50% ethanol. Tissues were sectioned at 5 μm thickness, rehydrated, and stained with hematoxylin and eosin (H&E) at the Pathology Core at Baylor College of Medicine. Microscopic images were taken on a ZEISS Axioscan scanner. Adipocyte sizes were quantified using AdipoQ software version 1.16.[107]

Generation of *UAS-ssp.HA.tag* transgenic fly lines

A transgenic construct that allows overexpression of a neutral 3xHA polypeptide with a signal sequence under the control of the UAS/GAL4 system[108] was generated as follows. We PCR amplified the rat Preproenkephalin signal sequence (SSP: MAQFLRLCIWLLALGSCLLATVQA) from pUAST-SSP::Aβ42[21] (a gift from Dr. Koichi Iijima) with primers to add a *Drosophila* codon optimized 3xHA tag (YPYDVPDYAYPYDVPDYAYPYDVPDYA) at its C-terminus. Restriction enzyme sites (BglII and XhoI) were also added for cloning purposes. The amplified fragment was first cloned into pGEM-T Easy plasmid (Promega) via TA cloning and subsequently shuttled to the pUAST.attB plasmid.[109] A Sanger sequence-validated clone was injected into the VK37 docking site on the 2nd chromosome.[110] This fly line is available upon request.

Figure design and illustration tools

All figures were made using Adobe Illustrator program. The graphical abstract and Figures 1A and 1E contain graphical elements created with Biorender.com.